

## N O T I C E

THIS DOCUMENT HAS BEEN REPRODUCED FROM  
MICROFICHE. ALTHOUGH IT IS RECOGNIZED THAT  
CERTAIN PORTIONS ARE ILLEGIBLE, IT IS BEING RELEASED  
IN THE INTEREST OF MAKING AVAILABLE AS MUCH  
INFORMATION AS POSSIBLE

THE UNIVERSITY OF MICHIGAN

COLLEGE OF ENGINEERING  
Department of Atmospheric and Oceanic Sciences  
Space Physics Research Laboratory

NSG-5281

(NASA-TM-80458) STATISTICAL STUDY OF  
PRECIPITATING ELECTRONS Final Report (NASA)  
64 p HC A04/MF A01 CSCL C4A

M81-31718

Unclass  
G3/46 27341

STATISTICAL STUDY OF PRECIPITATING ELECTRONS

Ernest G. Fontheim, K. Stasiewicz<sup>1</sup>, M. O. Chandler, R. S. B. Ong<sup>2</sup>

Space Physics Research Laboratory, University of Michigan

Ann Arbor, Michigan 48109

and

R. A. Hoffman

Laboratory for Planetary Atmospheres,

NASA Goddard Space Flight Center, Greenbelt, Maryland 20771



July 1981



# STATISTICAL STUDY OF PRECIPITATING ELECTRONS

Ernest G. Fonthelm, K. Stasiewicz<sup>1</sup>, M. O. Chandler, R. S. B. Ong<sup>2</sup>

Space Physics Research Laboratory, University of Michigan

Ann Arbor, Michigan 48109

and

R. A. Hoffman

Laboratory for Planetary Atmospheres,

NASA Goddard Space Flight Center, Greenbelt, Maryland 20771

<sup>1</sup>Now at Space Research Centre, Polish Academy of Sciences, Warsaw, Poland.

<sup>2</sup>Also at Department of Aerospace Engineering, University of Michigan, Ann Arbor, Michigan 48109

### Abstract

Energy spectra of precipitating electrons are fitted to the sum of three distributions, a power law, a Maxwellian and a Gaussian. This fitting procedure determines seven parameters which characterize the essential features of each spectrum. These characteristic parameters are used to carry out various studies involving precipitating electrons. It is shown that the absence of the power-law population from a particular spectrum is related to the softness of the precipitating primary flux, that the Maxwellian temperature and the Gaussian peak energy have a positive correlation the strength of which varies with local time, that the upward moving Gaussian population has a loss cone distribution, and that the one-dimensional velocity distribution parallel to the magnetic field occasionally displays a plateau or a hump on the tail.

## I. Introduction

The precipitation of charged particles at high latitudes represents one of the most interesting phenomena occurring in the ionosphere, because of the many interactions which these particles have undergone and which influence the shape of their spectra. A careful study of the characteristic features of their spectra is of special importance because those features represent the signature of their region of origin and of their acceleration mechanism and therefore contain information about physical processes occurring large distances away from the point of observation, frequently even deep in the magnetosphere. In addition, the precipitation spectrum determines the effect of the particles on the local ionosphere, such as ionization, emission of light, heating and the excitation of plasma instabilities.

Since the advent of in-situ measurements by instruments onboard space vehicles probably hundreds of millions of precipitating electron spectra have been obtained and duly stored on tape. Much valuable information contained in those spectra remains to be extracted. One practical way to deal with such a large data base is to associate with each spectrum a limited number of characteristic parameters and to base the study of the physics of precipitating electrons on those parameters. Obviously the choice of such characteristic parameters is critical for they must contain the important physical information carried by each spectrum. The parameterization of the electron fluxes lends itself not only to the interpretation of already existing data but can also be usefully included in the reduction of data currently being collected. The parameters of the various populations tell the investigator immediately the characteristic features of the observed spectra.

It is the purpose of this paper to describe a method for obtaining such a set of parameters for each spectrum and then to report the results of some studies.

The basis for this method is the recognition that the observed fluxes generally represent the superposition of several different populations and that each of these populations can be described in terms of certain characteristic parameters of an analytic function which is fitted to the observed fluxes. This has been done before by other investigators [e.g. Frank and Ackerson, 1971; Burch et al., 1976; Lin and Hoffman, 1979]. To our knowledge, however, no systematic effort has so far been made to parameterize large numbers of spectra on a production basis by means of a computerized fitting procedure and to use the parameters for investigations of the physical processes undergone by the fluxes.

In Section II the analytic expression selected by us is discussed. The characteristic parameters of each flux spectrum are determined by the fit of said analytic function to the measured spectrum. The computerized fitting procedure is briefly described in Appendix I. In Section III some of the present studies are briefly described. Section IV contains a summary of the results.

## II. Analytic Representation of Electron Energy Spectra

It has been pointed out in Section I that in order for a parametric representation of precipitation fluxes to be useful it is necessary that the selected parameters contain the important physical information carried by each spectrum. Based partly on earlier work by other authors and after extensive trials involving various different models we came to the conclusion that the electron spectra investigated by us so far can best be represented as a superposition of three populations given by the following expression:

$$\begin{aligned} \phi(E) &= aE^{-\alpha} + Cn \frac{E}{(kT)^{3/2}} e^{-E/kT} + EA e^{-[(E - E_0)/\Delta]^2} \\ &= \phi^{(1)}(E) + \phi^{(2)}(E) + \phi^{(3)}(E) \end{aligned} \quad (1)$$

Here  $C = (2m_e)^{-1/2} \pi^{-3/2}$  is a known constant and  $a$ ,  $\alpha$ ,  $n$ ,  $T$ ,  $A$ ,  $E_0$ , and  $\Delta$  are the parameters determined by the particular shape of each spectrum. The first term represents the well-known power-law spectrum which generally describes the combined backscattered and secondary electrons. Most of the electrons in the energy range from 200eV (the lowest energy measured by the Low Energy Electron Analyzer onboard the AE-D satellite) to 1keV frequently fall into this category. The second term is a Maxwellian with temperature  $T$ , while the third term represents a non-Maxwellian peak of Gaussian shape. Such peaks are characteristic of inverted-V spectra. The Gaussian distribution which has not been used in earlier works was introduced because the Maxwellian distribution gave only poor agreement with spectra containing near-monoenergetic peaks. If a Maxwellian fit were used for such spectra, the error was consistently larger than for spectra without such peaks. The details of the fitting procedure are presented in Appendix I. The analytic expression given by equation (1) is not necessarily the optimum model for all energy ranges, altitudes or even instruments. We are continuing to test different models (for example, to allow for two maxima).

The three populations which make up the resultant energy spectrum are believed to represent different physical processes undergone by the respective electrons. For example, the Gaussian term may be the result of a magnetic-field-aligned electric field accelerating the electrons into a near-monoenergetic beam. It is therefore logical to investigate the properties of such fields in terms of the parameters associated with the Gaussian rather than in terms of the total flux. Similarly, other investigations are best carried out by studying the properties of the individual populations, including of course any correlations between them.

Figures 1a and 1b show two examples both of which have Gaussian peaks. Yet, as these examples indicate, each of the three populations of equation (1) is not necessarily represented in every spectrum. The reason for the presence (or absence) of any of the three populations may shed light on the origin of the precipitating electrons and also on the interactions they have undergone. Figure 1a is a typical auroral spectrum, while the spectrum of Figure 1b almost looks like a magnetosheath spectrum, both as regards its shape as well as the value of the peak energy. Since the altitude of the spacecraft was at 620 km, the spacecraft was obviously not in the magnetosheath. However, Foster and Burrows [1977] have recently proposed that magnetosheath plasma, after penetrating to low altitudes inside the cleft, could diffuse to adjacent field lines, thereby contributing to the polar rain. Figure 1c shows the case of a spectrum which consists of a power-law and a Maxwellian population, but no Gaussian contribution.

The expression for the error, given in Appendix I, gives an upper bound of the mean square error of the logarithmic flux. In the vast majority of cases, this is of the order of  $10^{-2}$  or even less. The highest values encountered by us so far in a few examples are of the order of  $3 \times 10^{-1}$ . Considering this worst



case, the upper bound of the root mean square error is then  $5.5 \times 10^{-1}$ . This quantity would have to be compared with the smallest values of the logarithmic fluxes which are of the order of 4. Hence, we conclude that our analytical fit is remarkably good.

### III. Applications of the Characteristic Parameters

The examples reported in this section are based on data from the inverted-V events observed by the Low Energy Electron Analyzer (LEE) onboard the AE-D satellite. We have included 10s of data on either side of each inverted-V event. The list of inverted-V events was compiled by C. S. Lin (private communication) based on an analysis of the electron spectrograms.

There were two LEE detectors on the AE-D satellite, one at an angle of  $7^\circ$  with respect to the satellite axis and the other at an angle of  $60^\circ$ . The angles of the two detectors with respect to the geomagnetic field varied of course over an orbit. The flux component parallel to the geomagnetic field, however, was always the dominant one of the  $7^\circ$  detector, while the perpendicular component remained dominant for the flux measured by the  $60^\circ$  detector. Therefore, for purposes of identification, quantities relating to the  $7^\circ$  detector will be designated by the subscript  $\parallel$  and those relating to the  $60^\circ$  detector by the subscript  $\perp$ .

#### a) Some Properties of the Power-Law Population

One characteristic feature of the polar cap spectra is that in general they do not contain the power-law population at energies measured by the LEE instrument, i.e., above 200eV [c.f., Foster and Burrows, 1977]. The reason is evidently the softness of the precipitating primary flux. Based on a simple model of a constant field-aligned upward directed electric field above the satellite Evans [1974] has shown that the low energy down-streaming power-law population represents degraded backscattered primary electrons and secondary electrons which have been reflected downward by this electric field. This interpretation has been confirmed by the more rigorous treatment of Stamnes [1978, 1981]. The latter has shown that for a precipitating primary beam with Gaussian energy spectrum peaked at 500 eV the power-law spectrum lies below

about 120 eV which would make it invisible to the LEE instrument. Hence, the absence of the power-law population from the LEE spectrum can be considered a signature of soft primary precipitation characteristic of the polar rain. This is confirmed by Figures 2 and 3 in which the average peak energy of the Gaussian population and the average temperature of the Maxwellian with and without a power-law component are compared as functions of latitude at several local time sectors. The figures clearly show two interesting properties. The average peak energies and the average temperatures of the fluxes with power-law components are consistently higher than those without power-law components. Secondly, both the peak energy and the temperature have a minimum in the latitude range between  $80^\circ$  and  $85^\circ$  with the exception of the temperatures in the noon (10.5 - 13.5 hrs) and afternoon (13.5 - 16.5 hrs) sectors. The slight increase in the mean value of  $T_{||}$  toward the top latitude range in those two time sectors is as yet unexplained.

Table 1 lists the average and maximum values of the Gaussian peak energies and of the temperatures separately for the fluxes with and without power-law populations. Both the average and maximum values of the peak energies and of the temperatures of the fluxes without power-law populations are significantly lower than those of the fluxes with power-law populations. This is true of both the parallel and perpendicular components.

Figure 4 shows the average value of the power-law exponent  $\alpha$  for eight local time sectors, for both the parallel and perpendicular fluxes. In most cases the magnitude of  $\alpha$  has a maximum in the  $80-85^\circ$  latitude interval, indicating that the rate at which the power-law spectrum falls off generally increases toward higher latitudes. If the power-law population is made up of secondary and backscattered electrons, this behavior of  $\alpha$  is consistent with the increasing softness of the primary flux poleward of the auroral zone.

## b) Loss Cone Distribution of the Gaussian Beams

The Atmosphere Explorer satellites have the capability either to spin about an axis which is mostly perpendicular to the geomagnetic field or to fly despun as determined by ground command [Spencer et al., 1973]. The spinning orbits provide an opportunity for an investigation of the pitch angle variation of the various parameters. Figures 5 and 6 show a few examples of the pitch angle variations of the energy  $E_0$  and the temperature  $T$ . These figures show some interesting features. Because of the invariance of the magnetic moment all the downward hemispheres ( $0^\circ \leq \theta \leq 90^\circ$ ) are filled with Gaussian fluxes at those relatively low altitudes. The upward streaming fluxes have Gaussian populations in the pitch angle range from  $90^\circ$  to about  $110^\circ$  (in some cases even to larger values) and no Gaussian fluxes beyond, which is typical of loss cone distributions. Most of the downward streaming Gaussian fluxes are very nearly isotropic. Because of the loss cone distribution of the upward streaming Gaussian beams they can be assumed to consist of mirrored particles. It would therefore be of special interest to know the apex angle of the loss cone at the satellite altitude (and thus at all other altitudes). Unfortunately, this angle is difficult to determine from the data because the LEE spectrometer measures one spectrum per second, i.e., one spectrum only about every  $25^\circ$  of pitch angle. Hence, the data merely provide upper bounds of the apex angle (obtained from the largest pitch angle at which a Gaussian population has been observed) and lower bounds (obtained from the next larger pitch angle). Table 2 lists the mirror altitudes corresponding to both of these angles from data of AE-D orbit 635. The mirror points of most of the lower bounds lie below the surface of the earth and therefore provide no useful information. The lowest upper bound occurs at 127 km. Since the beam energy for this particular case is 2.35 keV, this altitude is close to where electrons of that energy are collisionally absorbed by the atmosphere [see e.g., Banks et al., 1974].

Hence, the apex angle of the loss cone of a 2.35 keV beam is indeed close to  $115^\circ$  at the altitude of 567 km (for an apex angle of  $114^\circ$  the mirroring altitude is 162 km - too high for collisional absorption of 2.35 keV electrons).

Figure 6 shows that the temperatures over the downward hemisphere ( $\theta < 90^\circ$ ) and outside the loss cone of the upward hemisphere ( $90 < \theta < 110$  appr.) are either isotropic or vary only slightly with pitch angle. Inside the loss cone the temperatures of the Maxwellian populations decrease (thus becoming highly anisotropic) with the minimum occurring parallel to the field line. The ratio of  $T_{\parallel}^{\text{down}}/T_{\parallel}^{\text{up}}$  can be as large as 2 (and sometimes even larger).

c) Correlation Between the Gaussian Peak Energy  $E_p$  and the Temperature T

The energy at the maximum of the Gaussian distribution appearing in equation (1) is given by

$$E_p = 1/2 (E_0 + \sqrt{E_0^2 + 2\Delta^2}).$$

A correlation analysis of T and  $E_p$  has been performed, and the results are summarized in Tables 3a and 3b. The correlation coefficients listed in Table 3a have been calculated separately for each cell in magnetic local time and invariant latitude, while the coefficients listed in Table 3b have been calculated for each magnetic local time sector for all latitudes above  $60^\circ$ . This breakdown is presented to study whether the correlation depends in some significant way on the magnetospheric region of origin of the fluxes. As the tables indicate, the correlation has a maximum during daytime and falls off toward the night. The fluxes carried by the Gaussian populations behave in a very similar way, i.e., the average Gaussian fluxes (averaged over the lifetime of AE-D) have a maximum during daytime and decrease toward the night in all latitude intervals. Therefore, as the intensity of the Gaussian fluxes decreases, their influence on the temperature declines compared with other mechanisms.

The linear relation between  $T$  and the peak energy  $E_p$  for all local times and latitudes has been obtained by a regression analysis which yields

$$\begin{aligned} T_{||} &= 0.604 + 0.400 E_{p||} \\ T_{\perp} &= 0.563 + 0.452 E_{p\perp} \end{aligned}$$

The standard error of the regression coefficient is 0.0086 for the parallel component and 0.0072 for the perpendicular one. 45% of the variance of  $T_{||}$  is explained by  $E_{p||}$ , and 59% of the variance of  $T_{\perp}$  is explained by  $E_{p\perp}$ . Burch et al. [1976] have anticipated the correlation between  $E_p$  and  $T$  based on an examination of a small sample of spectra. Lin and Hoffman [1979] performed regression analyses separately for each inverted-Y event. They obtained a set of values for the slope centered around a value of 0.2 which is half of our value. The reason for this discrepancy is believed to be due to the different definitions of  $T$  used by the two groups.

Several years ago Whalen and McDiarmid [1972] suggested that there may be a distributed source of cold electrons throughout the acceleration region. The beam which has fallen through the entire potential drop would then act as a heat source of the lower energy population through collective effects [see for example, Shapiro, 1963], thus resulting in a correlation between the peak energy and the temperature of the Maxwellian population travelling parallel to the beam. Those Maxwellian particles travelling upward inside the loss cone, on the other hand, have probably been scattered up by the ambient electrons or ions and have thereby been cooled. Since the heat transfer rate due to this mechanism is proportional to the flux intensity of the beam, it is therefore also consistent with the reduced correlation between  $T$  and  $E_p$  observed during nighttime as discussed above.

#### d) Some Properties of the One-Dimensional Velocity Distribution

The shape of the one-dimensional electron velocity distribution is of special interest for plasma physical reasons. In particular, if there is a hump on its tail, the plasma may be unstable. If the hump is being steadily supplied with new particles, then the instability can saturate at a non-equilibrium quasi-steady state of plasma turbulence which leads to anomalous transport effects.

The existence of such effects has recently been deduced from stormtime data in the auroral zone [Fontheim et al., 1978]. Another interesting consequence of plasma turbulence is the emission of a characteristic spectrum of electrostatic and electromagnetic waves. The one-dimensional distribution is defined as

$$F(v_z) = \int_{-\infty}^{\infty} dv_x \int_{-\infty}^{\infty} dv_y f(v_x, v_y, v_z).$$

where  $f(v_x, v_y, v_z)$  is the three-dimensional velocity distribution. For many applications the distribution of interest is the one-dimensional velocity distribution parallel to the geomagnetic field  $\vec{E}_0$  which is given by

$$F(v_{||}) = \int_0^{2\pi} d\psi \int_0^{\infty} dv_{\perp} v_{\perp} f(v_{||}, v_{\perp}, \psi) \quad (2)$$

where  $\psi$  is the azimuth in the plane perpendicular to  $\vec{E}_0$ . The formal dependence of  $f(v_{||}, v_{\perp}, \psi)$  on the azimuth  $\psi$  is included for generality. In most real situations the distribution is expected to be cylindrically symmetric about  $\vec{E}_0$ . Kaufmann and collaborators [Kaufmann et al., 1976, 1978a,b; Kaufmann, 1980] have discussed the significance of the one-dimensional distribution function in great detail and have also examined the compatibility of their observed distributions with various acceleration mechanisms.

Unfortunately, most instruments do not measure the three-dimensional velocity distribution. The usually observed quantity is the flux as a function of energy  $E$  in a solid angle element about a given direction, i.e.,

$$\phi(E, \theta, \psi) dE \sin\theta d\theta d\psi$$

where  $\phi(E, \theta, \psi)$  has the dimensions  $(\text{length})^{-2} (\text{time})^{-1} (\text{energy})^{-1} (\text{solid angle})^{-1}$  and where  $\theta$  is the pitch angle. The desired three-dimensional velocity distribution  $f(v_{||}, v_{\perp}, \psi)$  is related to the flux  $\phi(E, \theta, \psi)$  by the expression

$$\begin{aligned} f(v_{||}, v_{\perp}, \psi) v_{\perp} dv_{||} dv_{\perp} d\psi &= \frac{\phi(E, \theta, \psi)}{v} \frac{mv_{\perp}}{\sqrt{v_{||}^2 + v_{\perp}^2}} dv_{||} dv_{\perp} d\psi \\ &= \phi(E, \theta, \psi) \frac{mv_{\perp}}{v_{||}^2 + v_{\perp}^2} dv_{||} dv_{\perp} d\psi \end{aligned} \quad (3)$$

where  $f(v_{||}, v_{\perp}, \psi)$  has the dimensions  $(\text{length})^{-3} (\text{velocity})^{-3}$ . In using this expression for  $f(v_{||}, v_{\perp}, \psi)$  in the calculation of the one-dimensional distribution  $F(v_{||})$  the flux  $\phi(E, \theta, \psi)$  has to be understood in the sense that the parameters entering into  $\phi(E, \theta, \psi)$ , as given by equation (1), must be considered to be functions of the pitch angle  $\theta$ .

The integration appearing in equation (2) is carried out numerically. While the lower limit of the integration over  $v_{\perp}$  can be taken as zero as required (since the integrand vanishes at  $v_{\perp} = 0$  according to equation 3), the upper limit of the numerical integration is restricted to the largest value of  $v_{\perp}$  for which a flux measurement exists for a fixed  $v_{||}$ , which is given by

$$(v_{\perp})_{\max} = \text{MIN} [v_{||} \tan \theta_u, (2E_{\max}/m - v_{||}^2)^{\frac{1}{2}}],$$



where  $\theta_u$  is the closest pitch angle to  $90^\circ$  at which a spectrum was measured and  $E_{\max}$  is the maximum energy the instrument detects (20 keV in the case of the LEE).

If  $(m/2) v_{||}^2 < \text{MAX}(E_o, T_b)$ , then most of the contributions to the integral in equation (2), with the integrand given by (3) and (1), come from the energy range in the neighborhood of  $E_o$  and  $T$ . Since the integrand decreases exponentially with  $E$  for  $E > \text{MAX}(E_o, T_b)$ , the error introduced in the integral by leaving out the interval above  $(v_{\perp})_{\max}$  is negligible provided

$$\frac{m}{2} [(v_{\perp})_{\max}^2 + v_{||}^2] \gg \text{MAX}(E_o, T).$$

If  $m v_{||}^2 / 2 > \text{MAX}(E_o, T)$ , then the error is negligible provided

$$\frac{m}{2} [(v_{\perp})_{\max}^2 + v_{||}^2] \gg \frac{m}{2} v_{||}^2.$$

The numerical integration of equation (2) has to be carried out for each value of  $v_{||}$ . The largest value of  $v_{||}$  for which  $F(v_{||})$  has been computed is  $6 \times 10^9$  cm/s which corresponds to an electron energy of 10 keV. The range  $0 \leq v_{\perp} \leq (v_{\perp})_{\max}$  is divided into 100 equidistant intervals resulting in a set of  $v_{\perp k}$ . For any fixed value of  $v_{||}$  the pitch angles corresponding to the set of  $v_{\perp k}$  are given by  $\theta_k = \tan^{-1} \frac{v_{\perp k}}{v_{||}}$ , and the values of the seven parameters entering into the flux expression (1) are obtained by linear interpolation between their fitted values at the pitch angles at which the flux has been measured. The value of the integrand is then calculated at each  $v_{\perp k}$  with the energy given by  $(m/2)(v_{||}^2 + v_{\perp k}^2)$ . Thus the numerical integration appearing in equation (2) can be carried out with the integrand given by equation (3). This integration must of course be repeated for a series of values of  $v_{||}$  to obtain  $F(v_{||})$  in the desired range of its argument.

In order to get good coverage from a range of values of  $v_{\perp}$  for the integral in equation (2) the one-dimensional distribution function  $F(v_{\parallel})$  must be calculated from spinning orbits by using data from both LEE instruments. Since there were only relatively few spinning orbits of AE-D, it was only possible to obtain a limited number of one-dimensional distribution functions. Some examples of different cases are presented in Figures 7 through 10. Figure 7 shows a high velocity tail of a completely stable distribution. Figures 8 and 9 are two examples of plateau formation indicating the existence of an instability at a prior time, and Figure 10 shows a hump.

An important special case exists when the three-dimensional velocity distribution  $f(v_{\parallel}, v_{\perp}, \psi)$  is spherically symmetric, i.e., if it depends on the velocity components  $v_{\parallel}$  and  $v_{\perp}$  only through  $v^2 = v_{\parallel}^2 + v_{\perp}^2$ . It is well known that if a three-dimensional velocity distribution is spherically symmetric (or isotropic), then the one-dimensional distribution as defined above can have at most one maximum and this is located at  $v = 0$ , irrespective of the shape of the three-dimensional distribution. Thus a hump on the tail of the one-dimensional velocity distribution is automatically excluded if the three-dimensional distribution is spherically symmetric, even if the three-dimensional distribution has a hump as a function of energy. Although this is a well known property of distribution functions, a brief proof of this theorem will be presented in Appendix II because of the importance of this property for electron precipitation fluxes.

As is indicated in Figure 5, the hump in the energy distribution may be isotropic over the downward hemisphere. The above mentioned property of spherically symmetric three-dimensional distributions applies separately to  $v_{\parallel} \geq 0$  and  $v_{\parallel} \leq 0$ , and therefore the one-dimensional velocity distribution has no peak on the downward tail. Since all spectra examined by us have pitch angle distributions similar to that shown in Figure 5, it may be generally true that

at low altitudes the one-dimensional velocity distributions of precipitating electrons generally do not have a hump on the high velocity tail. This is expected to be the case at altitudes below some critical altitude  $z_c$  at which the beam particles with the largest pitch angles first start to mirror. Hemispherical isotropy is also the reason why Kaufmann et al. [1978a;b] did not detect any secondary peaks, aside from a few exceptions.

As has been mentioned above, the existence of a hump on the tail of the one-dimensional distribution function may give rise to a plasma instability which, according to quasilinear plasma theory, has the effect of flattening the peak into a plateau on the tail of the distribution. Papadopoulos and Coffey [1974a], however, have shown that under certain conditions a parametric instability is excited, the so-called oscillating two-stream instability. This instability has the effect of transferring wave energy out of the wave regime of phase velocities near the beam velocity (corresponding to frequencies near the plasma frequency) into the regime of much lower frequency ion fluctuations. This limits the growth of wave amplitudes of those waves with phase velocities near the beam velocity which strongly interact with the beam. As a result the beam is stabilized against quasilinear diffusion. According to Papadopoulos and Coffey [1974a] the condition for stability against quasi-linear diffusion of the beam is

$$(n_b/n_e)^{2/3} (v_b/\Delta v_b)^{7/3} (v_e/v_b)^{2/3} (M/m)^{1/3} < 10^{-2} (k_m^2 \lambda_D^2)^{1/3} \quad (4)$$

where  $n_b$  and  $v_b$  are the beam density and velocity respectively,  $n_e$  is the ambient electron density,  $\Delta v_b$  the velocity spread of the beam,  $v_e$  the thermal velocity of the ambient electrons,  $M$  and  $m$  the ion and electron masses respectively,  $k_m$  the wavenumber with the maximum growth rate for the parametric instability, and  $\lambda_D$  the Debye length. In none of the cases examined by us was this condition satisfied. As a result, the humped distribution function shown in Figure 10 is not expected

to stabilize into a quasi-steady state of plasma turbulence.

In those cases where the above condition is satisfied the growing ion density fluctuations give rise to an enhancement of the parallel resistivity of the plasma. Papadopoulos and Coffey [1974b] have shown that in this case the anomalous resistivity  $\eta_a$  can be expressed in terms of an effective collision frequency  $\nu_{eff}$ ,

$$\eta_a = \frac{4\pi}{\omega_p^2} \nu_{eff} \quad (5)$$

where  $\omega_p$  is the electron plasma frequency of the ambient plasma. The effective collision frequency is given by Papadopoulos and Coffey [1974b]

$$\nu_{eff} = 0.376 \alpha \left( \frac{n_b}{n_e} \right) \left( \frac{v_b}{v_e} \right)^2 \left( \frac{\Delta v_b}{v_b} \right) \omega_p \quad (6)$$

where  $n_b$  is the density of the beam,  $n_e$  the density of the ambient electrons,  $v_b$  the beam velocity,  $v_e$  the thermal velocity of the ambient electrons,  $\Delta v_b$  the velocity spread of the beam, and  $\alpha$  is a factor of order unity.

Once the one-dimensional distribution  $F(v_{||})$  is known, one can determine whether it has a maximum (i.e., a hump) on the tail, and, if so, fit another function of  $v_{||}$  to this hump, designated by  $F_b(v_{||})$ , representing the one-dimensional distribution of near mono-energetic beam particles. The density of the beam electrons is then given by  $n_b = \int_{-\infty}^{\infty} F_b(v_{||}) dv_{||}$ , the beam velocity  $v_b$  is the velocity value at the maximum, and the velocity spread  $\Delta v_b$  is simply the standard deviation of the distribution  $F_b(v_{||})$ . The ambient density  $n_e$  and the ambient temperature  $T_e$  (which determines the thermal velocity  $v_e$ ) are being measured by other instruments. Hence, all parameters entering in equation (6) can either be measured or calculated, and the anomalous resistivity can thus be obtained for every spectrum which has a one-dimensional hump and satisfies condition (4).

#### IV. Summary

A method for the computerized parametrization of electron energy spectra has been outlined together with a few examples of studies based on these derived parameters. It was shown that the presence of the power-law population is linked to the energy of the precipitating primary beam. This is consistent with the view that the power-law population is composed of secondaries and backscattered primaries. A detailed correlation study between  $E_p$  and  $T$  showed that these two parameters are positively correlated and that the correlation is significantly stronger during local daytime than at nighttime. This effect may be related to the fact that the Gaussian fluxes also are larger during daytime and fall off toward the night. The one-dimensional velocity distributions parallel to the geomagnetic field are decreasing with  $v_{||}$  in the great majority of cases, i.e., they represent stable configurations. In some cases, however, they show a plateau on the tail, indicating an instability at an earlier time. A few hump-on-the-tail distributions were also detected.

Acknowledgements: We wish to thank Jolanta Grygorczyk and Maryam Shahnava for computer programming assistance and Eszter Gombosi for having carried out the statistical analyses for this study.

## References

- Banks, P. M., C. R. Chappell and A. F. Nagy, A new model for the interaction of auroral electrons with the atmosphere: spectral degradation, back-scatter, optical emission, and ionization, J. Geophys. Res., 79, 1459, 1974.
- Burch, J. L., S. A. Fields, W. B. Hanson, R. A. Heelis, R. A. Hoffman and R. W. Janetzke, Characteristics of auroral electron acceleration regions observed by Atmosphere Explorer C, J. Geophys. Res., 81, 2223, 1976.
- Evans, D. S., Precipitating electron fluxes formed by a magnetic field-aligned potential difference, J. Geophys. Res., 79, 2853, 1974.
- Fontheim, E. G., R. S. B. Ong, R. G. Roble, H. G. Mayr, M. J. Baron, W. H. Hoegy, V. B. Wickwar, R. A. Vondrak and J. A. Ionsen, Effect of anomalous transport coefficients on the thermal structure of the storm time auroral ionosphere, J. Geophys. Res., 83, 4831, 1978.
- Foster, J. C., and J. R. Burrows, Electron fluxes over the polar cap 2. Electron trapping and energization on open field lines, J. Geophys. Res., 82, 5165, 1977.
- Frank, L. A., and K. L. Ackerson, Observations of charged particle precipitation into the auroral zone, J. Geophys. Res., 76, 3612, 1971.
- Kaufmann, R. L., Electrostatic wave growth: secondary peaks in a measured auroral electron distribution function, J. Geophys. Res., 85, 1713, 1980.
- Kaufmann, R. L., D. N. Walker and R. L. Arnoldy, Acceleration of auroral electrons in parallel electric fields, J. Geophys. Res., 81, 1673, 1976.
- Kaufmann, R. L., P. B. Dusenbery, B. J. Thomas and R. L. Arnoldy, Auroral electron distribution function, J. Geophys. Res., 83, 586, 1978a.
- Kaufmann, R. L., P. B. Dusenbery and B. J. Thomas, Stability of the auroral plasma: parallel and perpendicular propagation of electrostatic waves, J. Geophys. Res., 83, 5663, 1978b.

- Lin, C. S., and R. A. Hoffman, Characteristics of the inverted-V event, J. Geophys. Res., 84, 1514, 1979.
- Papadopoulos, K., and T. Coffey, Nonthermal features of the auroral plasma due to precipitating electrons, J. Geophys. Res., 79, 674, 1974a.
- Papadopoulos, K., and T. Coffey, Anomalous resistivity of the auroral plasma, J. Geophys. Res., 79, 1558, 1974b.
- Shapiro, V. D., Nonlinear theory of the interaction of a monoenergetic beam with a plasma, Sov. Phys. JETP, 17, 416, 1963.
- Spencer, N. W., L. H. Brace and D. W. Grimes, The Atmosphere Explorer spacecraft system, Radio Sci., 8, 267, 1973.
- Stamnes, K., A theoretical investigation of the interaction of auroral electrons with the atmosphere, Thesis, Department of Astro-Geophysics, University of Colorado, 1978.
- Stamnes, K., On the two-stream approach to electron transport and thermalization, J. Geophys. Res., 86, 2405, 1981.
- Whalen, B. A. and I. B. McDiarmid, Observations of magnetic-field-aligned auroral electron precipitation, J. Geophys. Res., 77, 191, 1972.

TABLE 1: COMPARISON OF TEMPERATURES AND PEAK ENERGIES IN THE  
PRESENCE AND ABSENCE OF POWER-LAW FLUXES.

	Temperature (keV)		Peak energy (keV)	
	Average	Maximum	Average	Maximum
$\phi_H^{(1)} = 0$	0.571	11.978	1.035	3.637
$\phi_H^{(1)} \neq 0$	2.224	19.990	2.645	11.950
$\phi_L^{(1)} = 0$	0.581	4.705	0.996	3.653
$\phi_L^{(1)} \neq 0$	2.344	19.782	2.753	14.353



TABLE 2

Upper and Lower Bounds of Mirror Heights of  
Electrons on the Surface of the Loss Cone

UT	Pitch * Angle	Spacecraft Altitude (km)	Mirror ** Altitude (km)	Beam *** Energy (keV)	Upper (U) or Lower (L) Bound
13126	110°	529	249	4.58	U
127	134°	530	0	0	L
131	128°	534	0	0	L
132	104°	536	399	4.98	U
140	92°	544	541	5.68	U
141	116°	545	71	0	L
146	121°	550	0	0	L
147	97°	552	518	4.82	U
155	99°	560	503	1.73	U
156	123°	561	0	0	L
160	139°	566	0	0	L
161	115°	567	127	2.35	U
170	105°	577	419	4.61	U
171	130°	578	0	0	L
175	132°	582	0	0	L
176	108°	583	355	4.72	U
185	112°	593	251	4.77	U
186	137°	594	0	0	L

\* The pitch angle is taken with respect to the downward direction.

\*\* If the mirror point would have fallen below the surface of the earth, it was recorded as 0 km altitude.

\*\*\* If no beam feature was present in the spectrum, the energy was recorded as 0 keV.

TABLE 3. CORRELATION COEFFICIENTS OF T AND E<sub>p</sub>

		a) by latitude and local time interval									
LAT	MLT Parallel Perpendicular	1.5-4.5	4.5-7.5	7.5-10.5	10.5-13.5	13.5-16.5	16.5-19.5	19.5-22.5	22.5-1.5		
60-65	Parallel	-	-	-	-	-	-	*	*		
	Perpendicular	-	-	-	-	-	-	0.7867	*		
65-70	Parallel	*	-	-	-	0.9070	0.8849	0.4530	0.3046		
	Perpendicular	*	-	-	-	0.6297	0.7949	0.5894	0.4180		
70-75	Parallel	0.9268	*	0.6664	-	0.9339	0.9271	0.6858	0.7004		
	Perpendicular	0.6102	*	*	-	0.9380	0.9678	0.7195	0.7558		
75-80	Parallel	0.9682	0.6962	0.9010	0.9726	0.7613	0.9703	0.9466	0.6906		
	Perpendicular	0.9615	0.6167	0.6069	0.8551	0.7501	0.9784	0.9722	0.8878		
80-85	Parallel	0.7930	0.8046	0.8490	0.8457	0.9030	*	0.5573	1.0000 <sup>1</sup>		
	Perpendicular	0.8951	0.8222	0.7981	0.9189	0.9145	0.9942	0.9097	-		

-: No cases in the cell.

\*: The value is non-significant.

1: 2 bases were detected.

## b) by local time sectors

LAT	MLT Parallel Perpendicular				
		0.2162	0.3656	0.9467	0.9365
60-65	Parallel	0.7291	0.2162	0.5763	0.9467
	Perpendicular	0.8278	0.3656	0.5513	0.9365
65-70	Parallel	0.5216	0.6258	0.9459	0.9687
	Perpendicular	0.6614	0.7226	0.9687	0.9687

## Figure Captions

- Figure 1. a) Example of an analytical fit of a spectrum consisting of the sum of a power-law, a Maxwellian, and a Gaussian distribution.
- b) Example of an analytical fit of a spectrum consisting of the sum of a Maxwellian and a Gaussian distribution.
- c) Example of an analytical fit of a spectrum consisting of the sum of a power-law and a Maxwellian distribution.

Figure 2. Variation of Gaussian peak energy with invariant latitude in eight local time sectors.

Figure 3. Variation of temperature with invariant latitude in eight local time sectors.

Figure 4. Variation of power-law exponent with invariant latitude in eight local time sectors.

Figure 5. Pitch angle variation of the Gaussian peak energy ( $E_0$ ). If a spectrum does not contain a near-monoenergetic peak (i.e., a Gaussian population),  $E_0$  is listed as zero. The left-hand ordinate scales refer to the solid curves and the right-hand ones to the dashed curves. The data were taken from AE-D orbit no. 635 in the altitude range from 556 km to 605 km, invariant latitude range from  $76^\circ$  to  $73^\circ$  and at MLT 20 hrs.

Figure 6. Pitch angle variation of the temperature (T). The left-hand ordinate scales refer to the solid curves and the right-hand ones to the dashed curves. The data were taken from AE-D orbit no. 635 and the same altitude, latitude and MLT as the data of Figure 2.

**Figure 7.** Plasma physically stable one-dimensional velocity distribution parallel to the geomagnetic field derived from observed electron energy spectra of AE-D orbit 635.

**Figure 8.** One-dimensional velocity distribution parallel to the geomagnetic field derived from observed electron energy spectra of AE-D orbit 647. The distribution presents a good example of plateau formation.

**Figure 9.** One-dimensional velocity distribution parallel to the geomagnetic field derived from observed electron energy spectra of AE-D orbit 647. The distribution presents a good example of plateau formation.

**Figure 10.** One-dimensional velocity distribution parallel to the geomagnetic field derived from observed electron energy spectra of AE-D orbit 635. The distribution shows a clear example of a hump-on-the-tail.

# ELECTRON DIRECTIONAL FLUX $\#/(cm^2 \cdot s \cdot ster \cdot keV)$

ORBIT: 635

UT: 13183 S

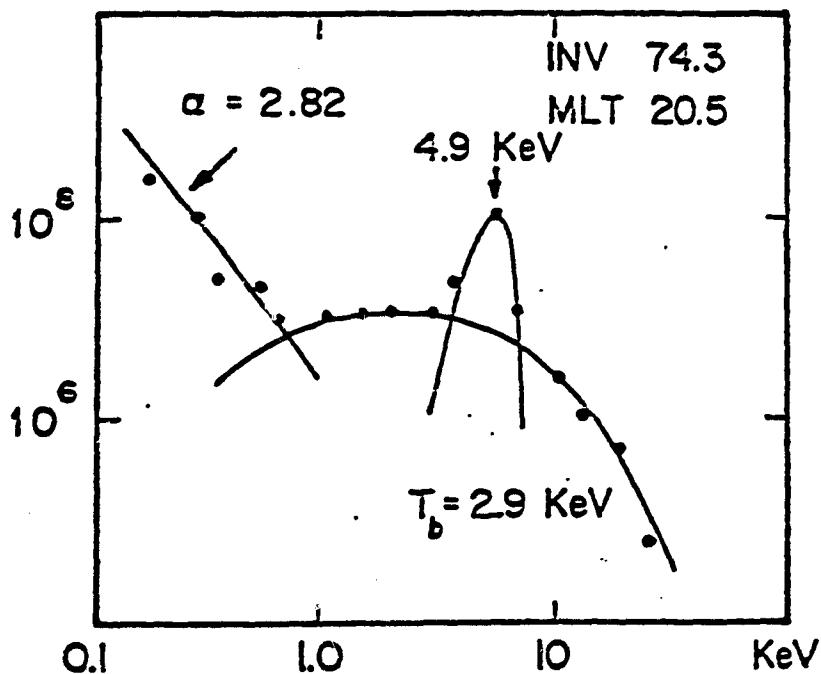


Figure 1a

ORBIT: 671

UT: 16326 S

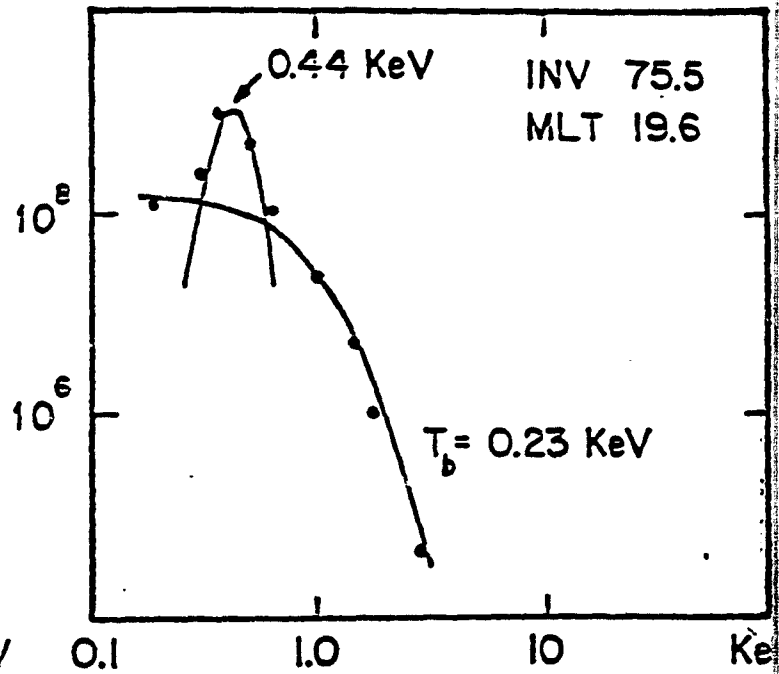


Figure 1b

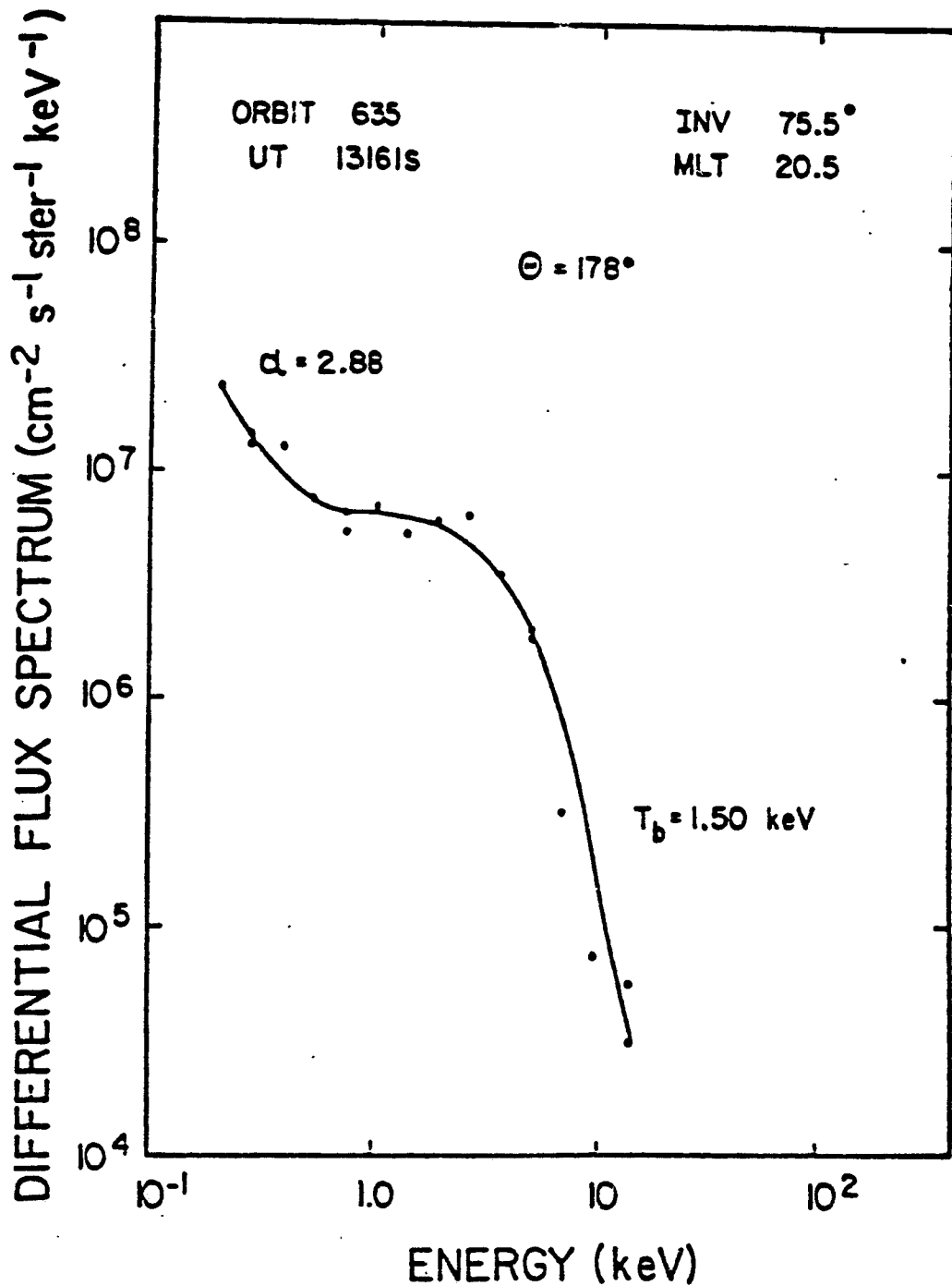


Figure 1c

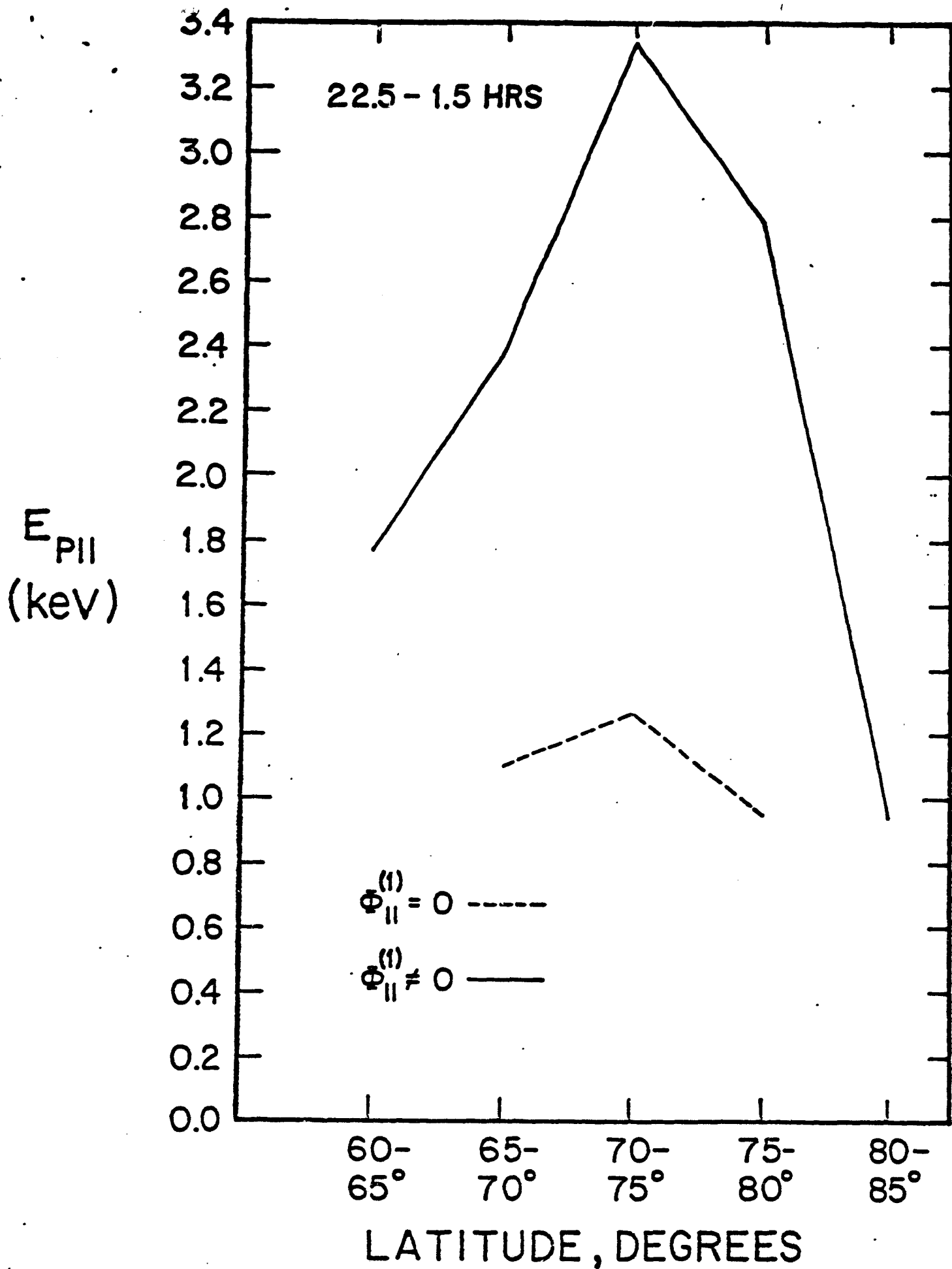


Figure 2a

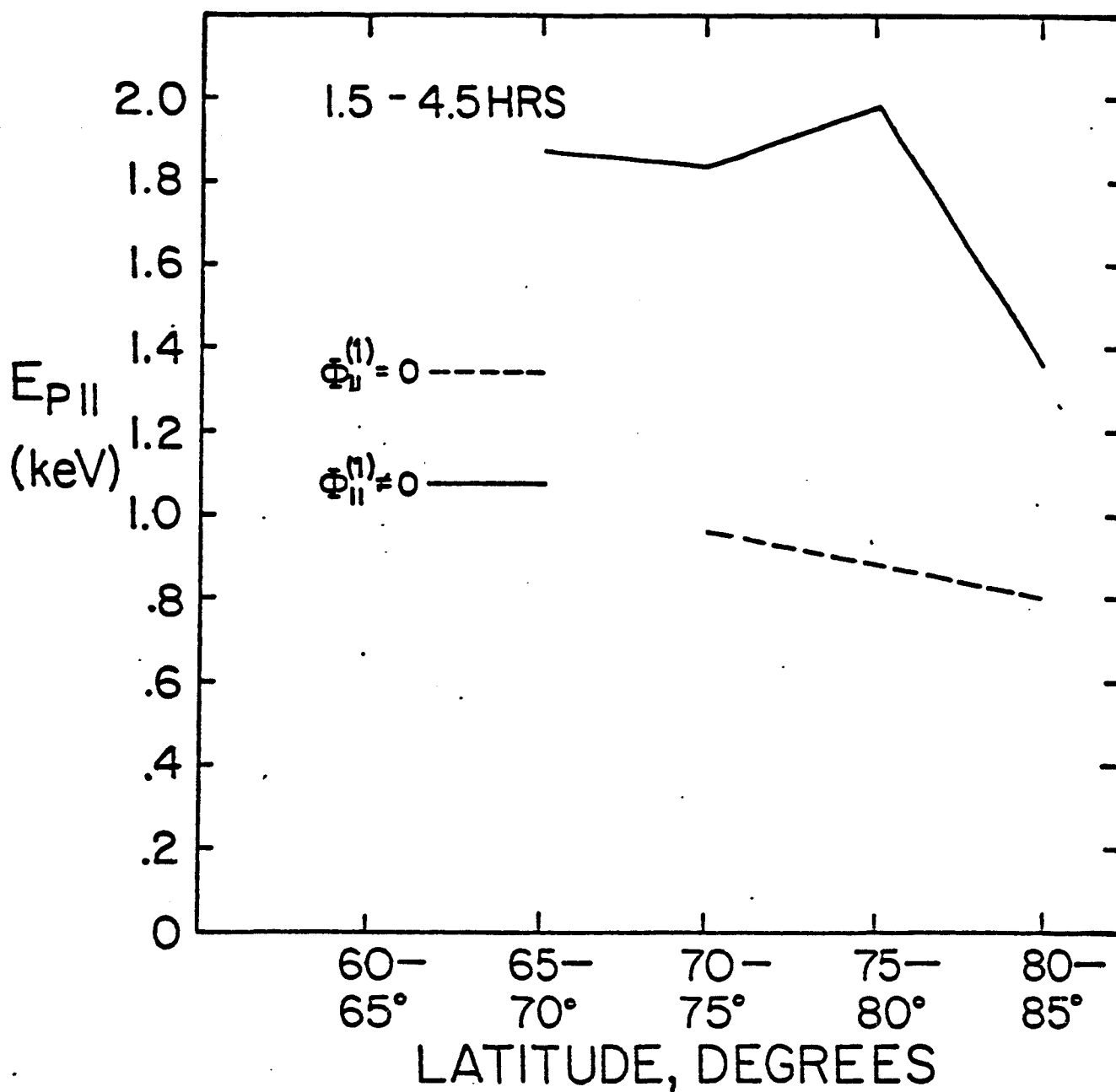


Figure 2b



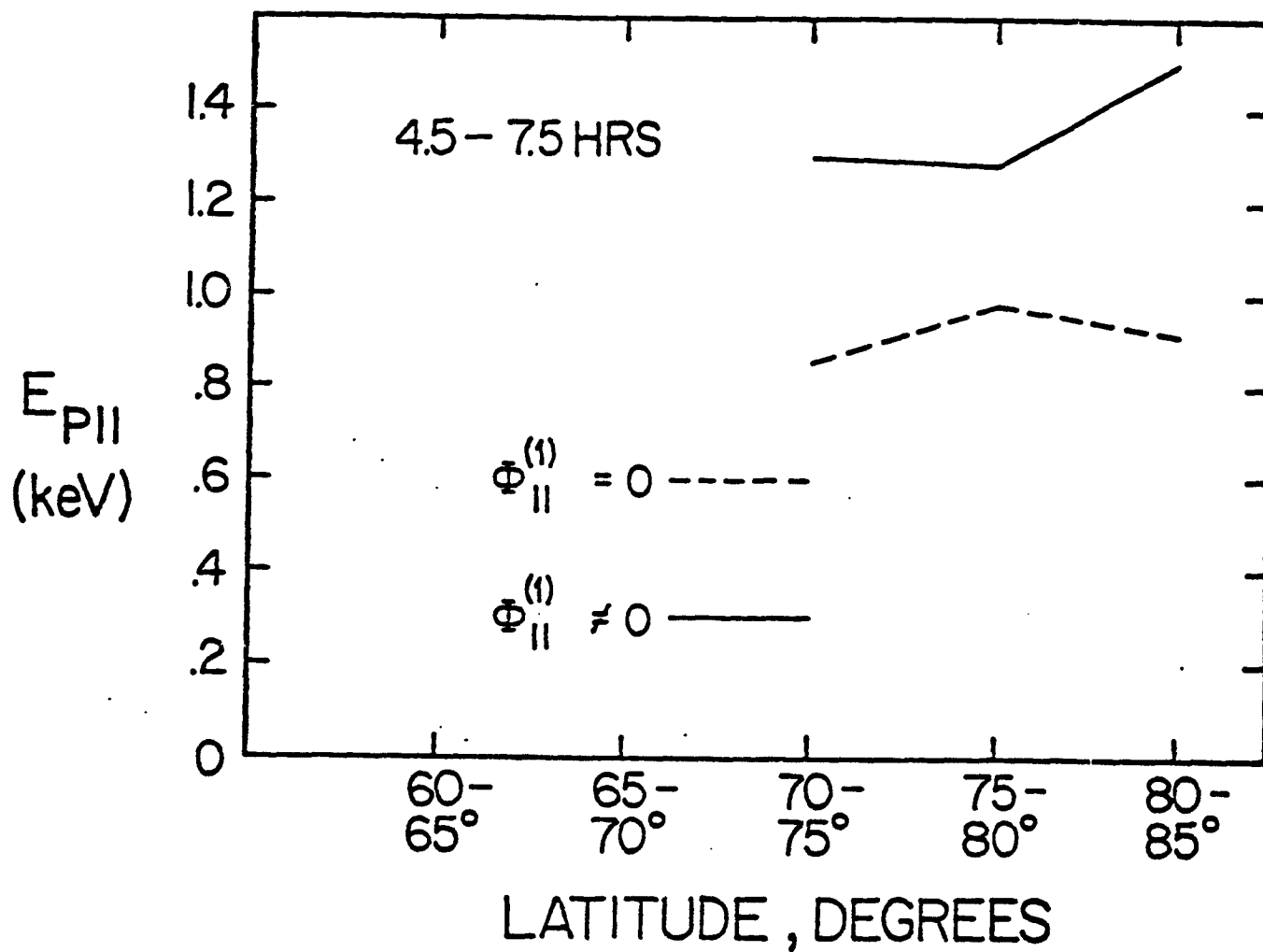


Figure 2c

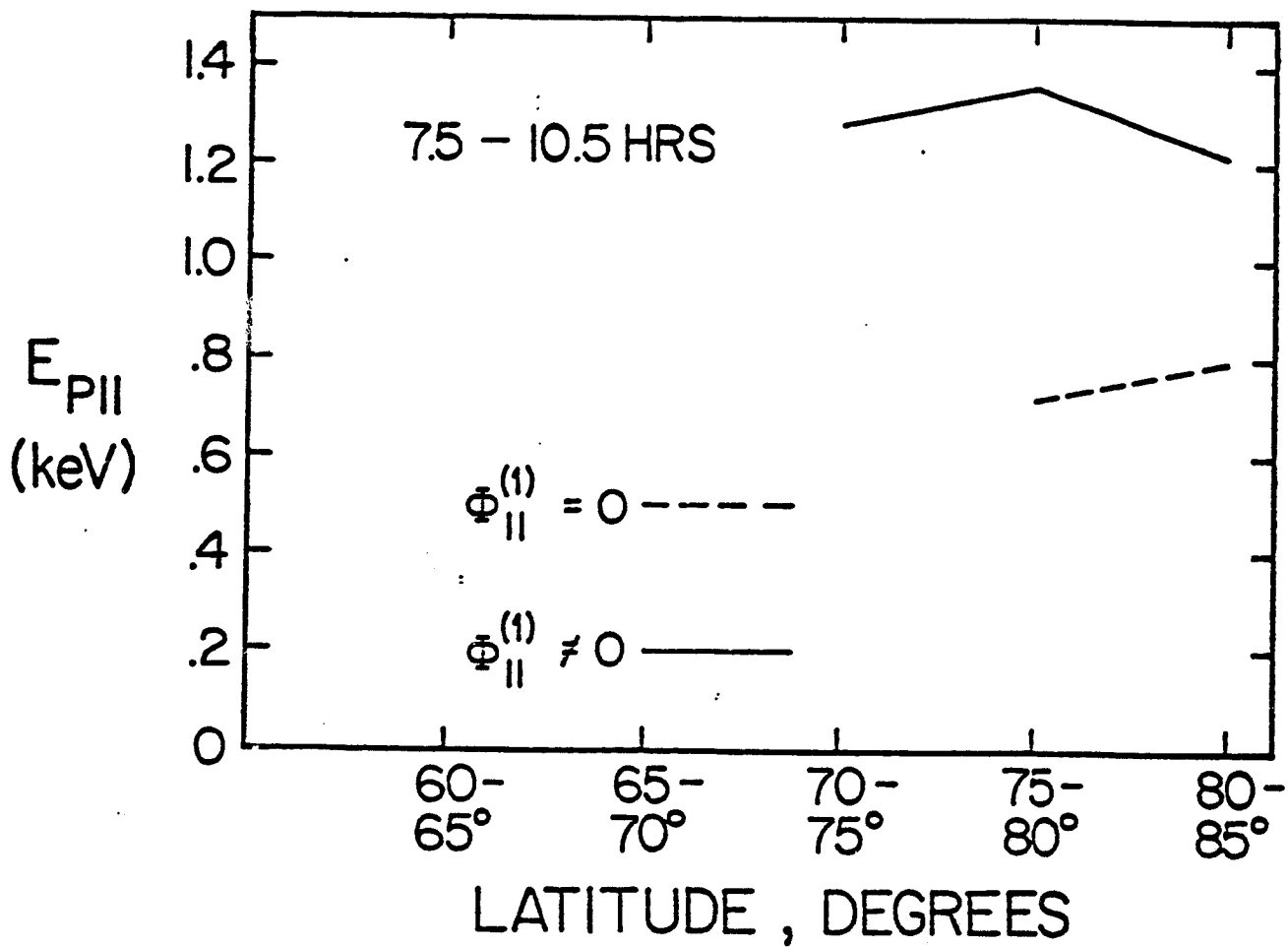


Figure 2d

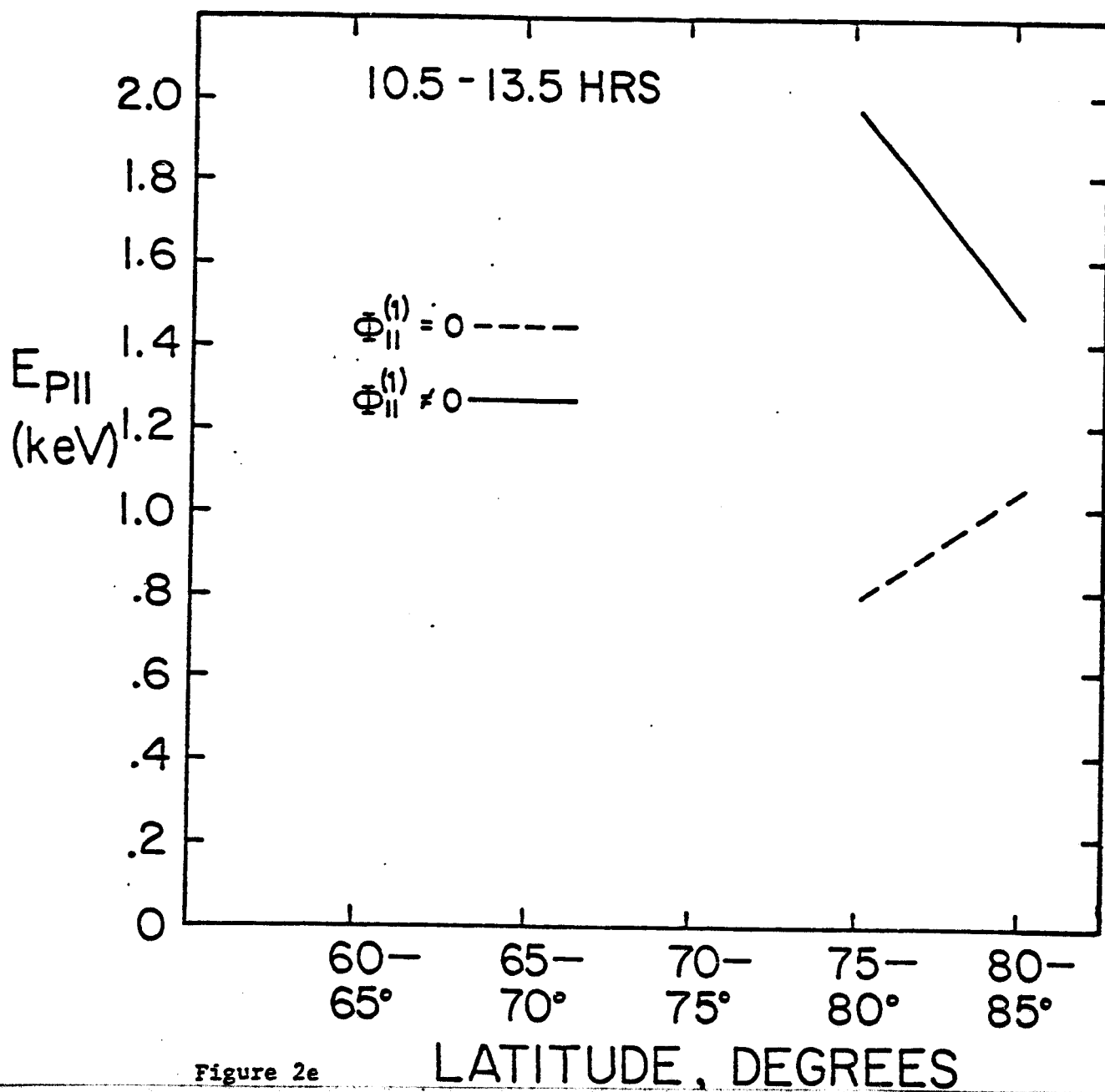


Figure 2e

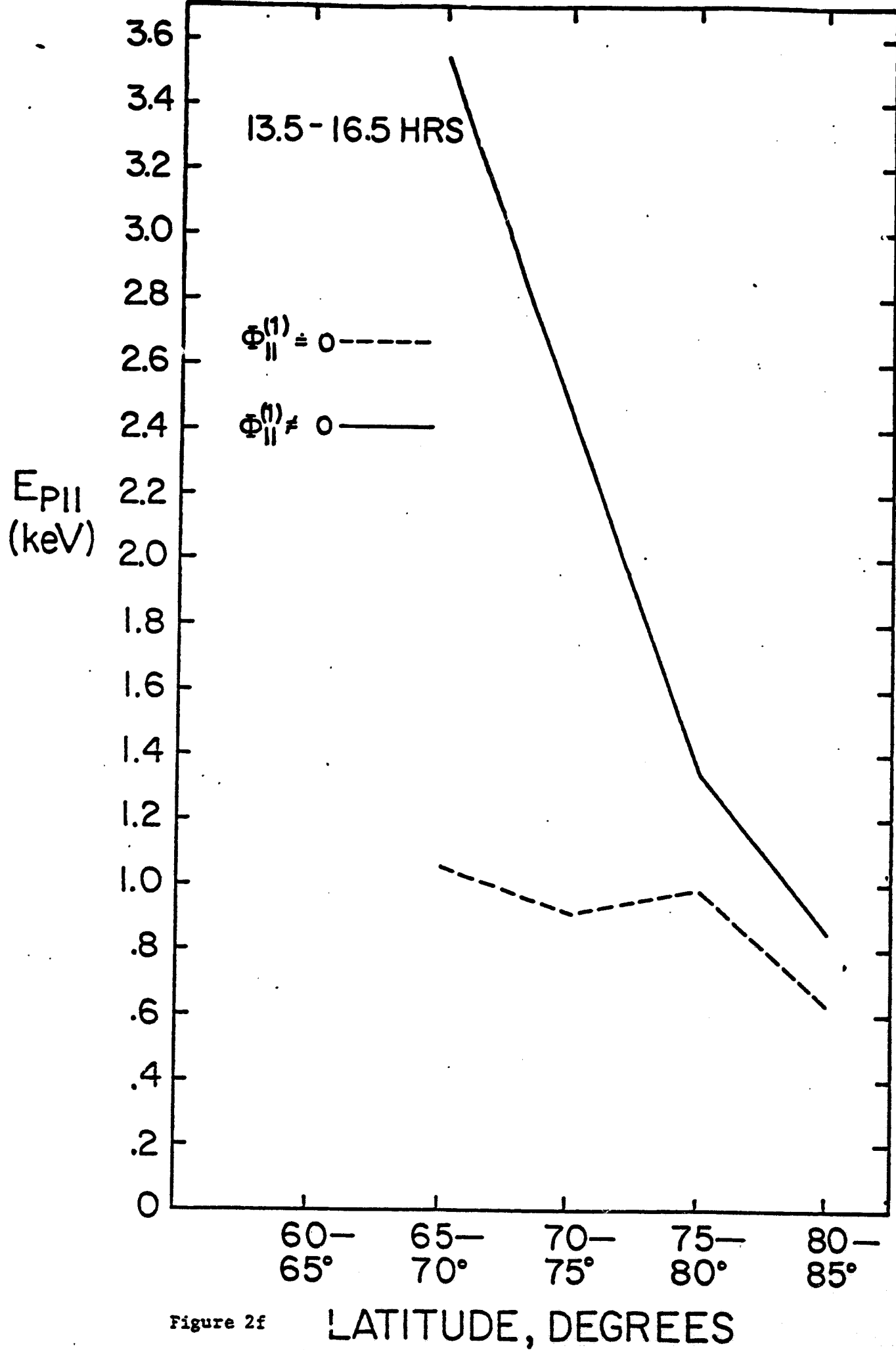


Figure 2f

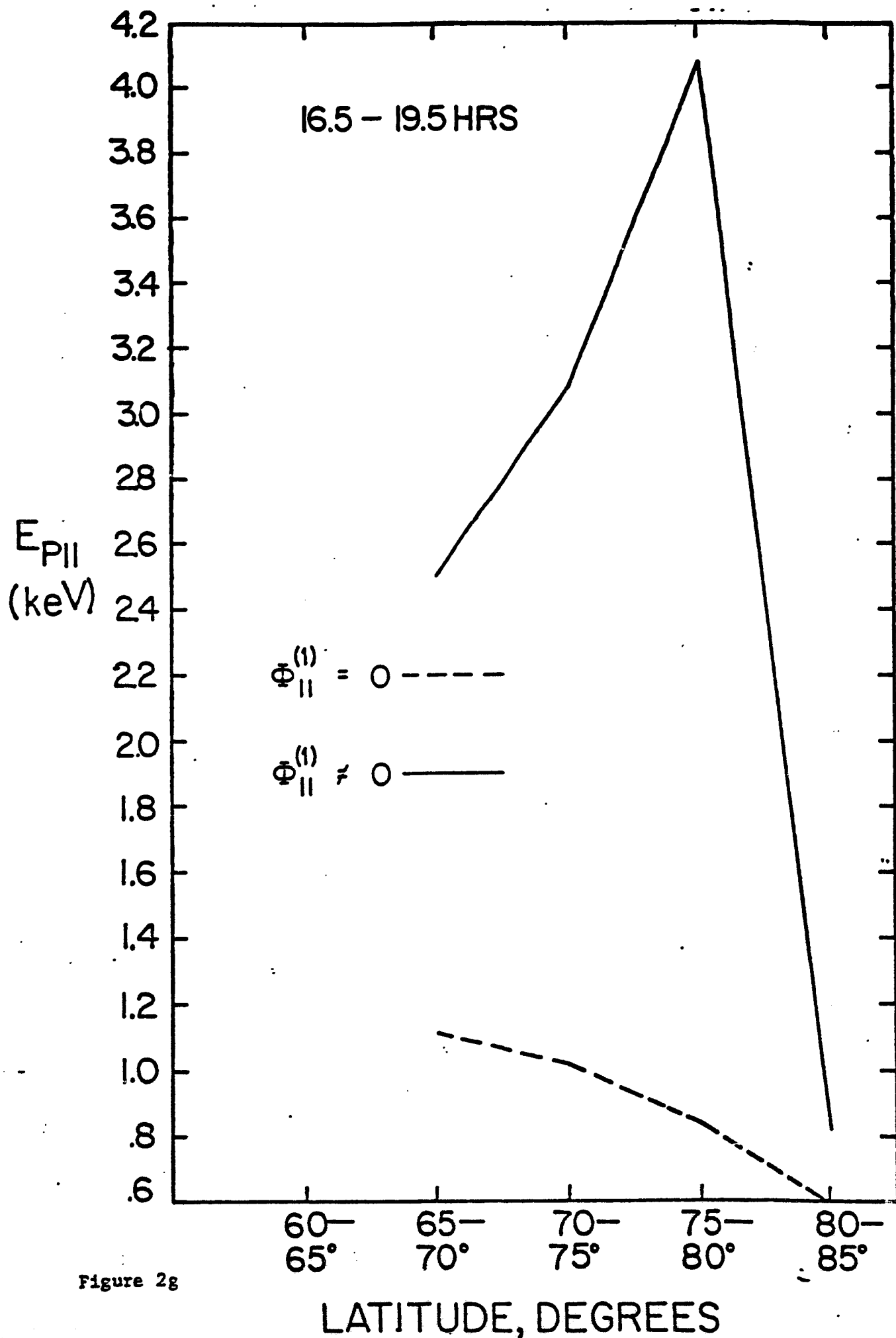


Figure 2g

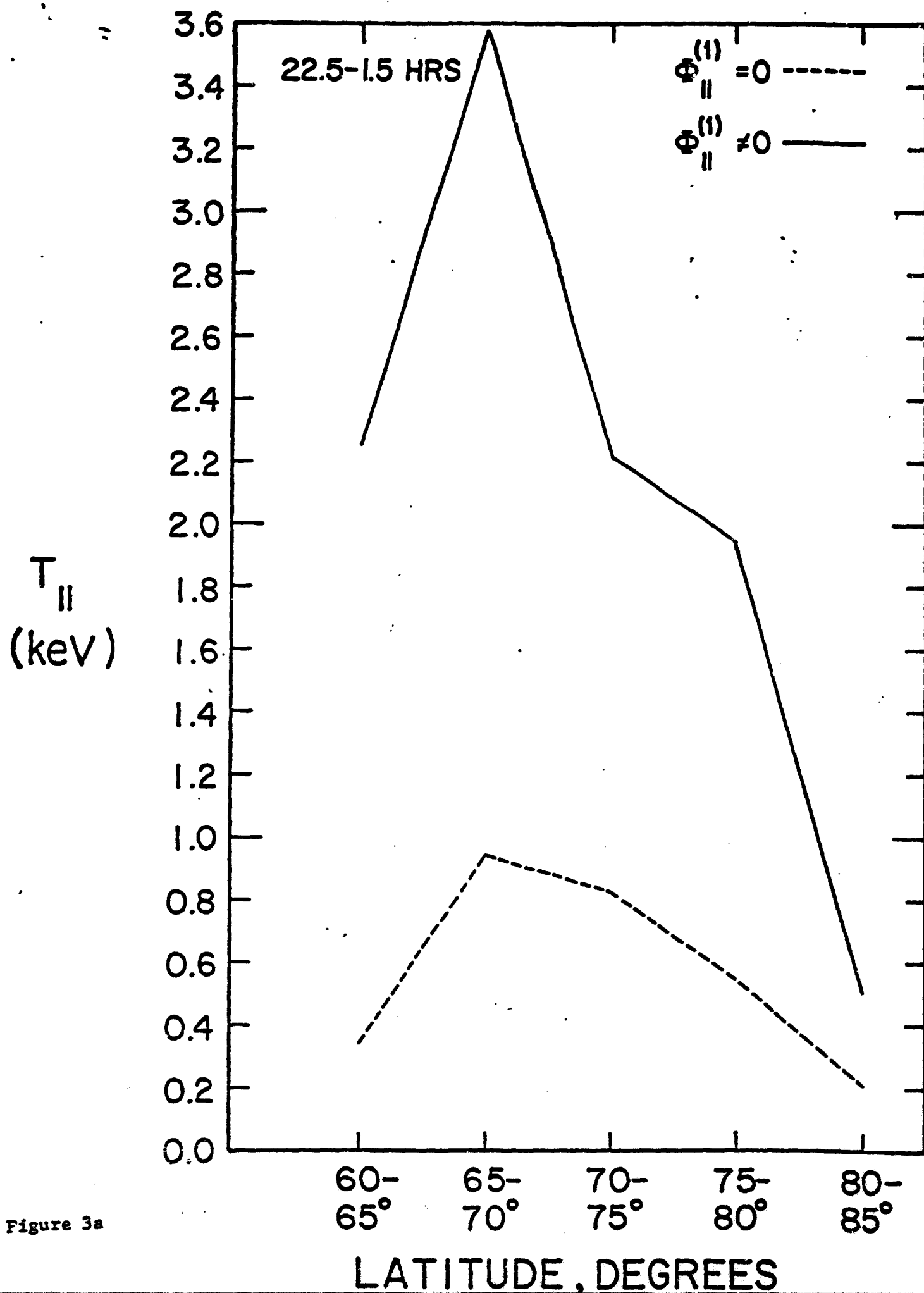


Figure 3a

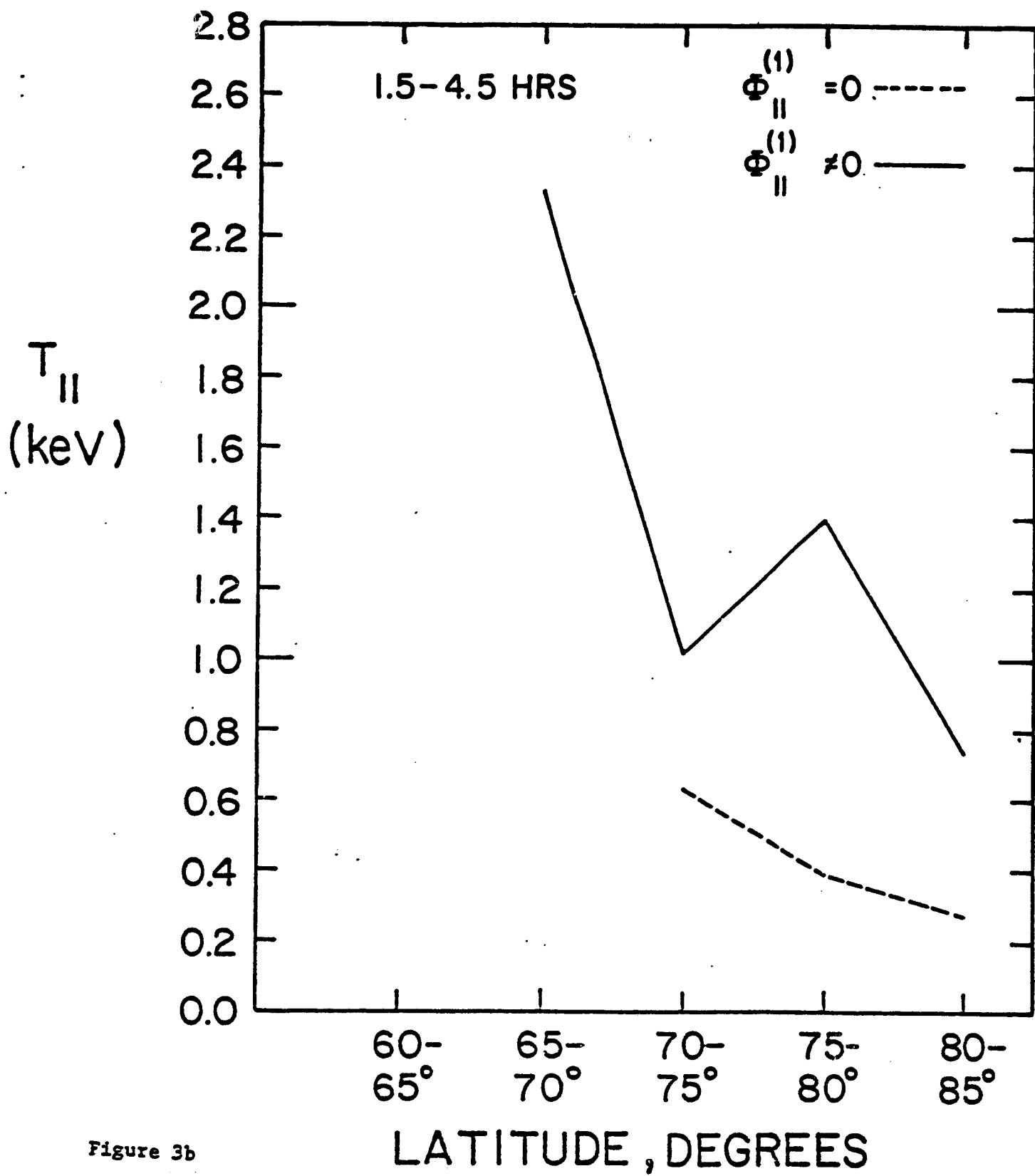
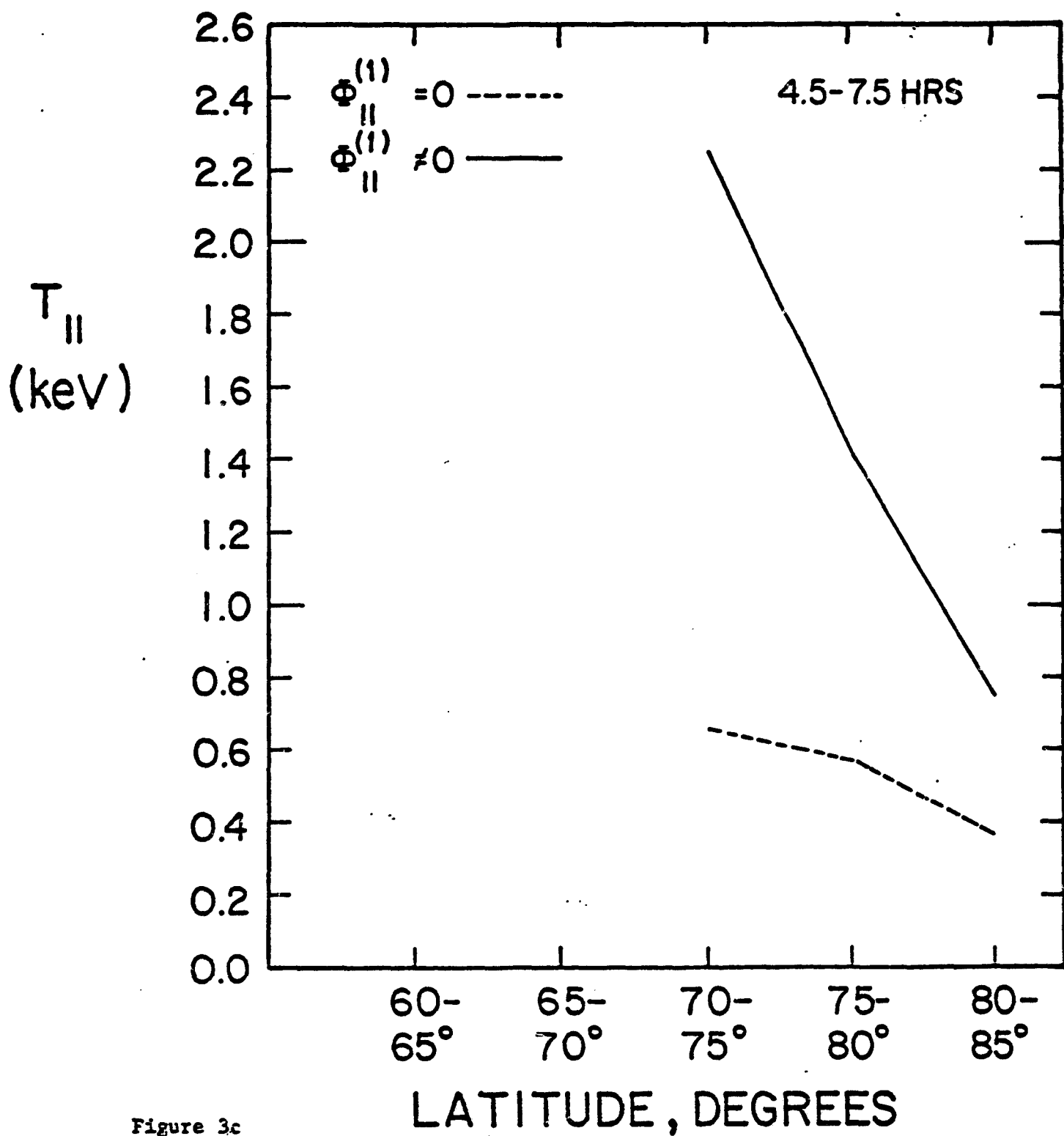


Figure 3b





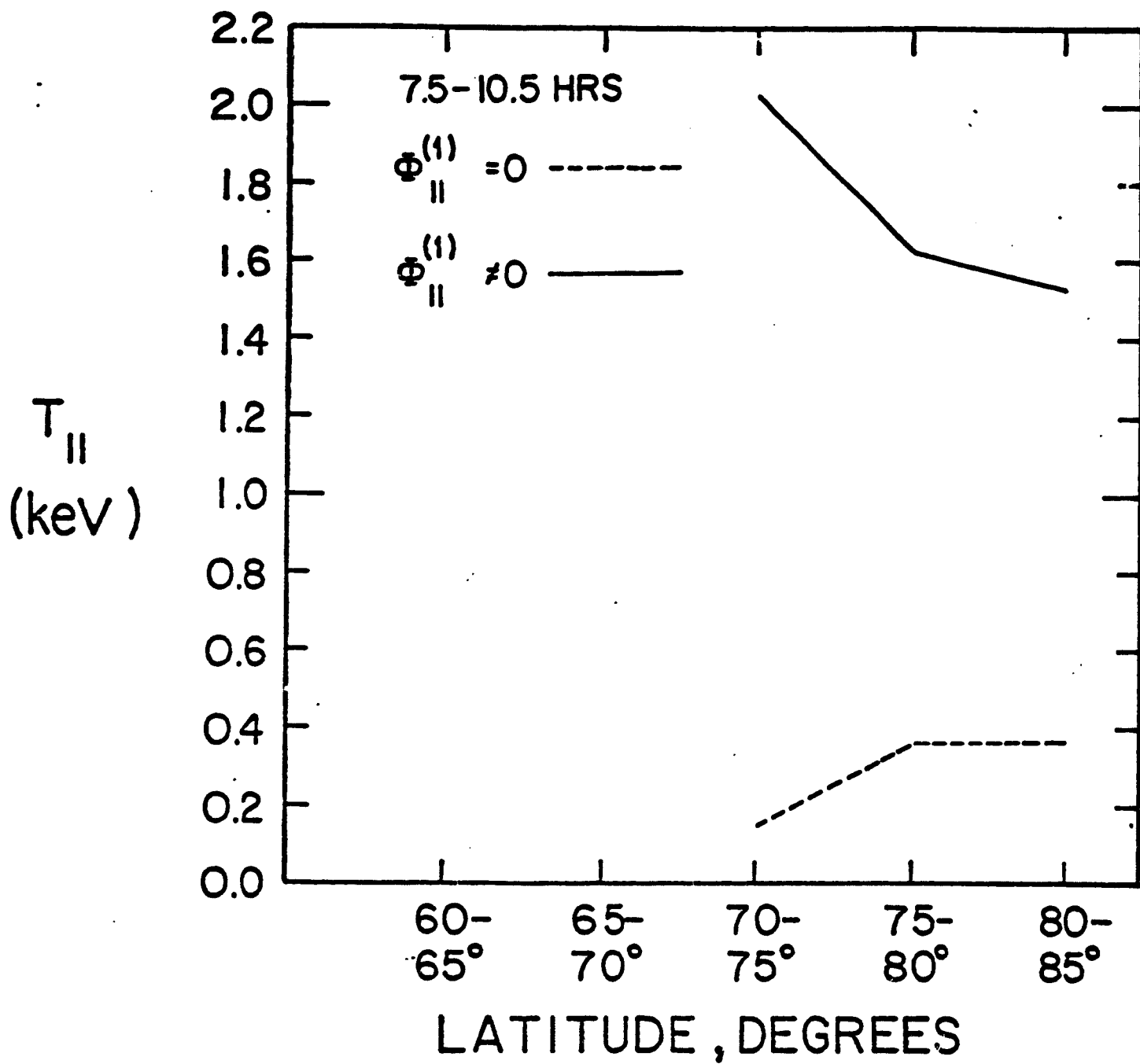


Figure 3d

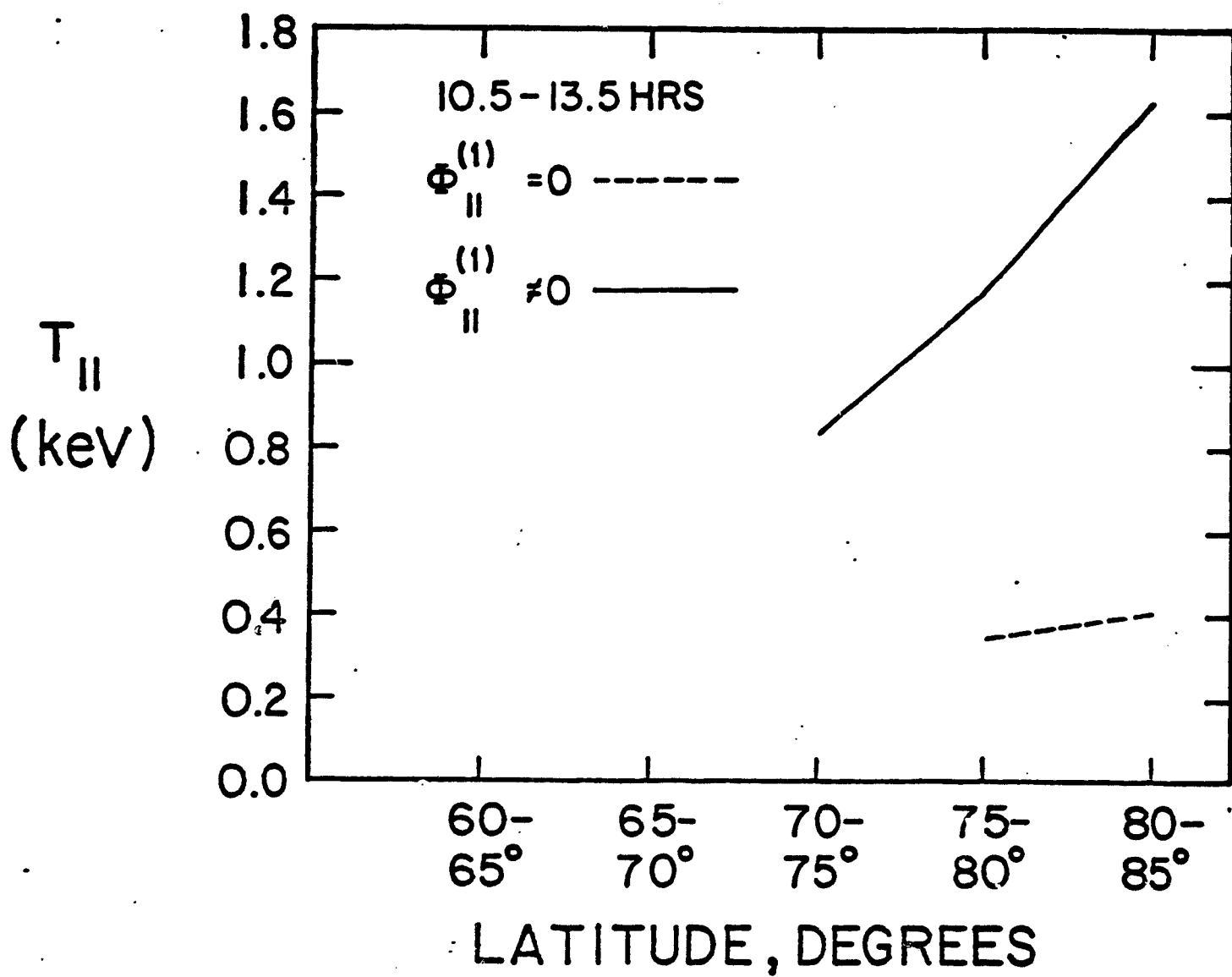


Figure 3e

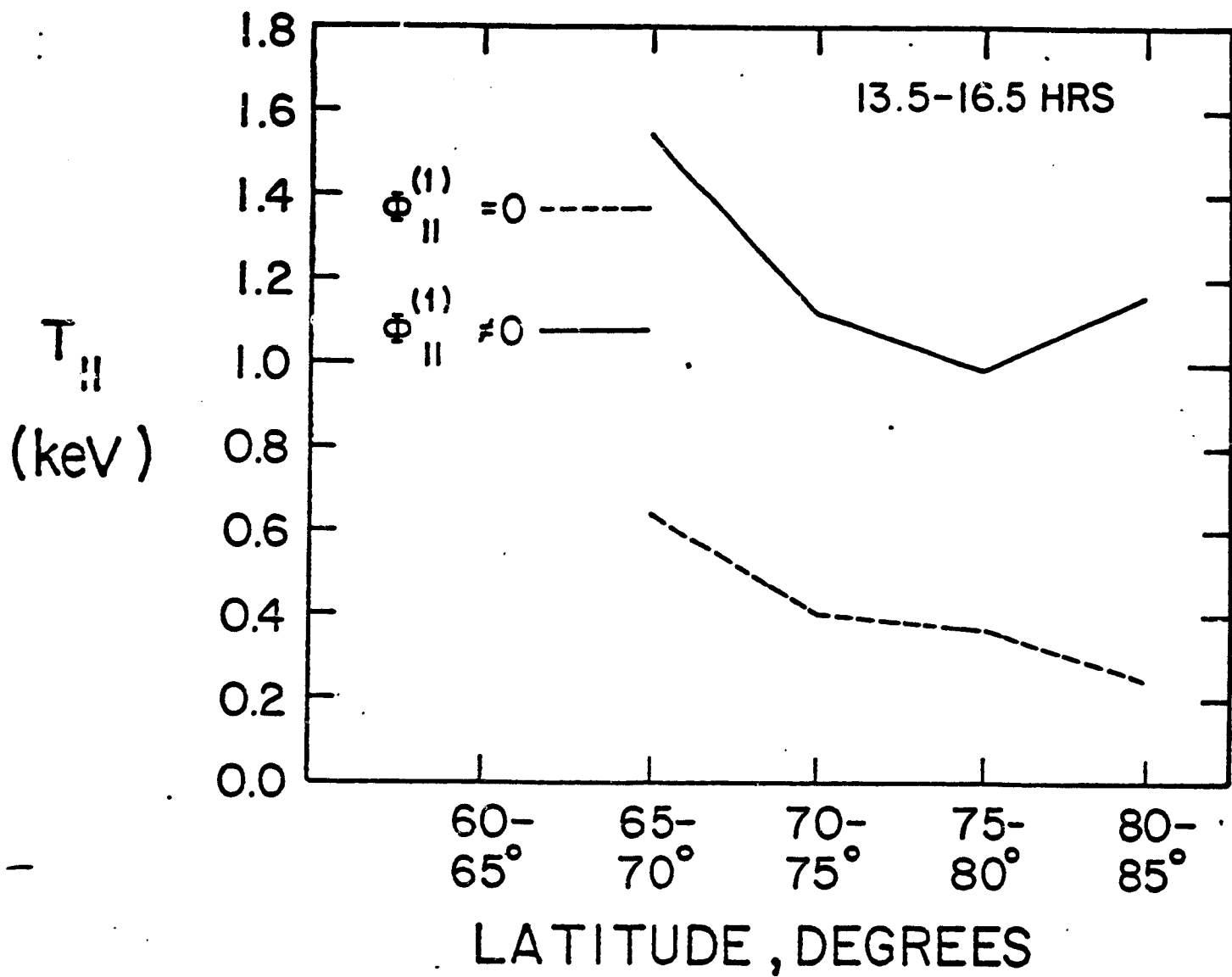


Figure 3f

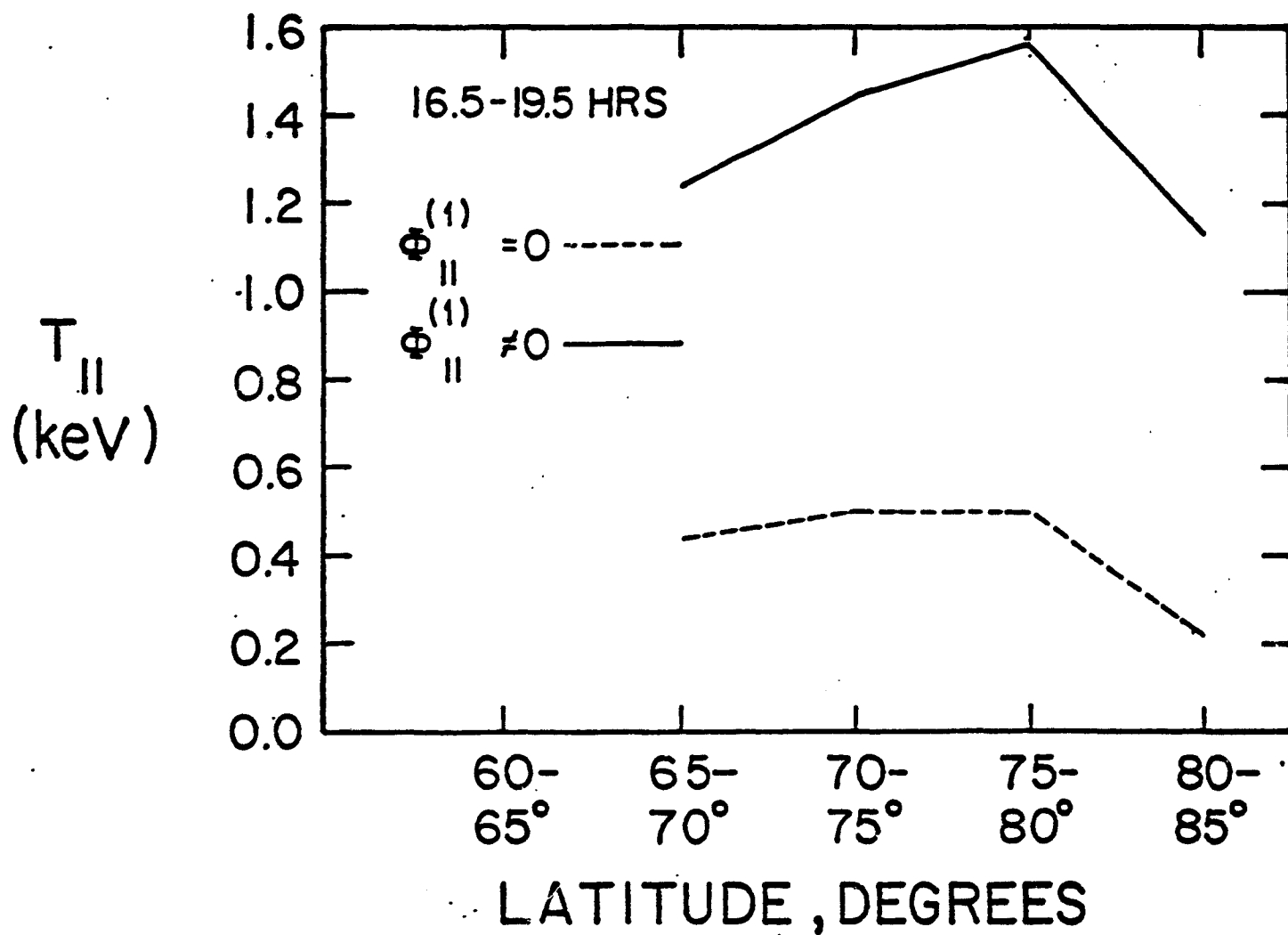


Figure 3g

$T_{\parallel}$   
(keV)

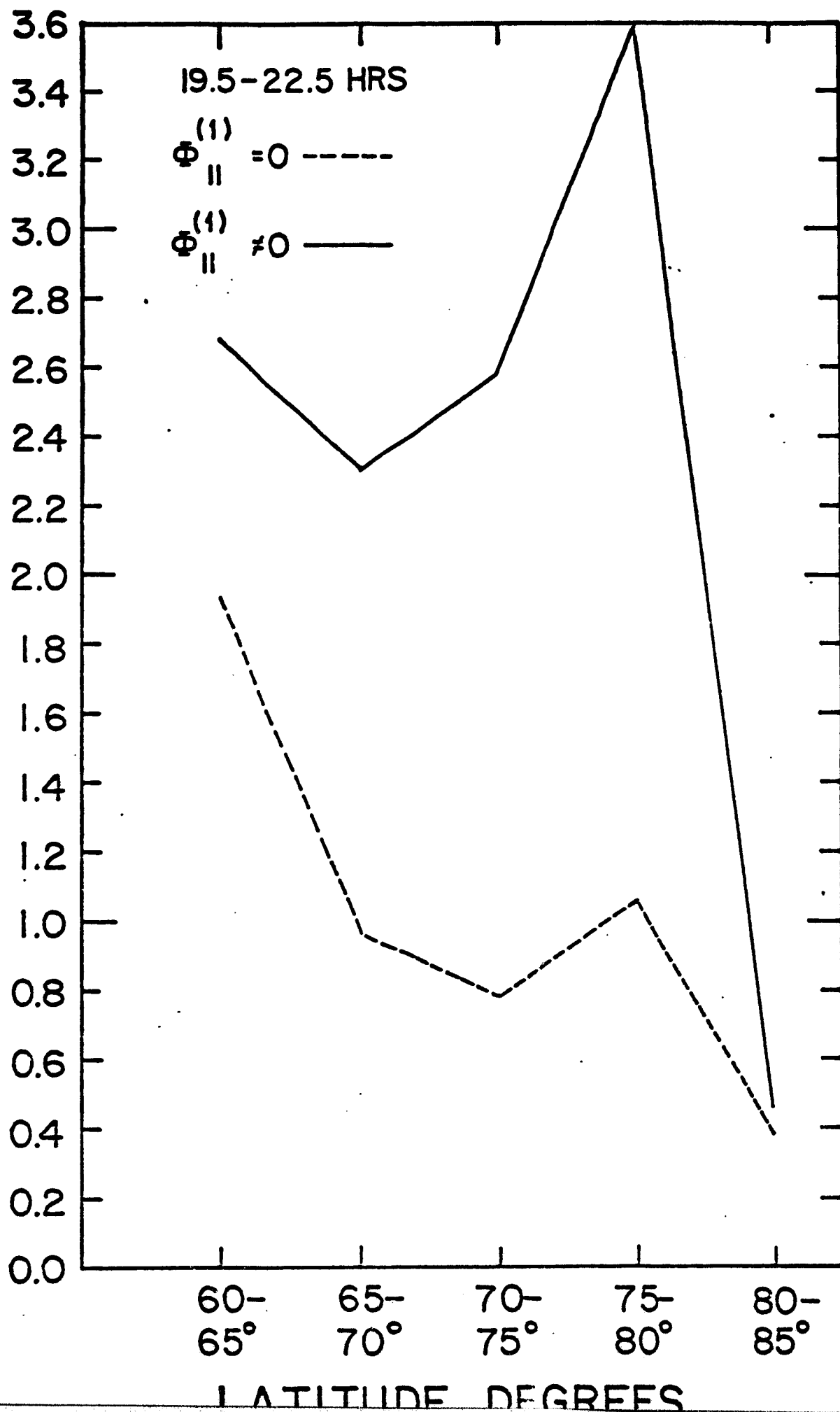


Figure 3h

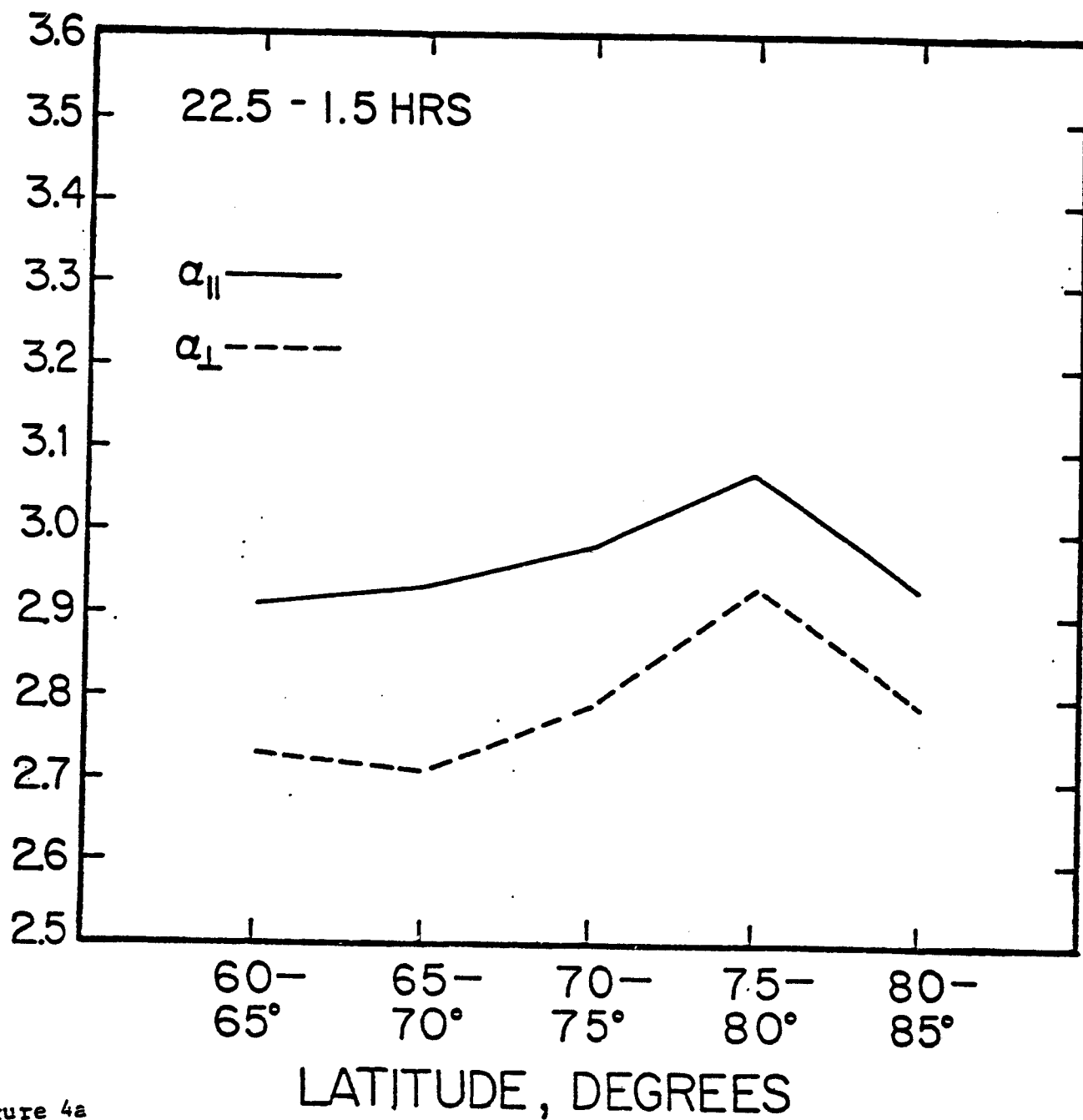


Figure 4a

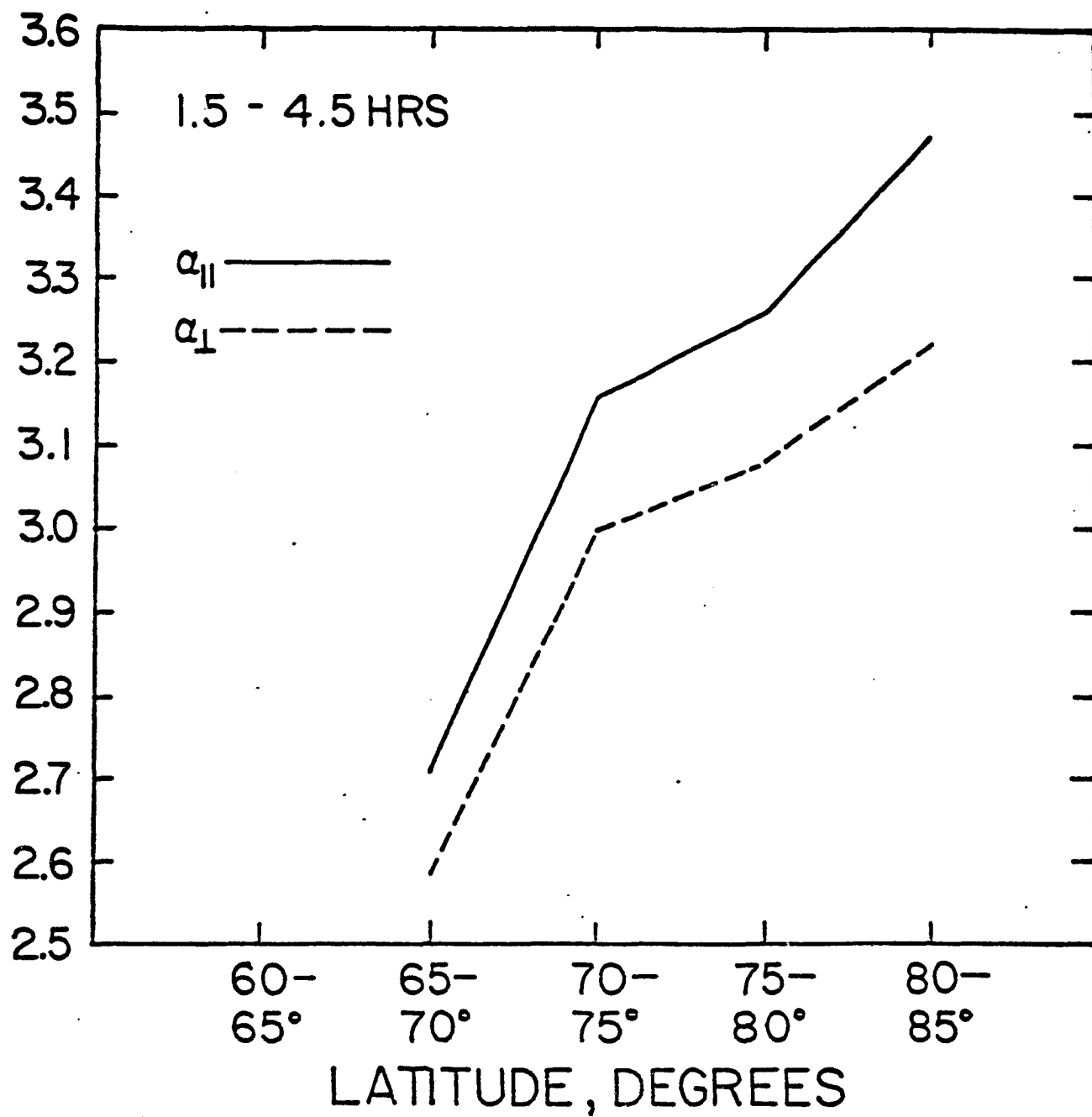


Figure 4b

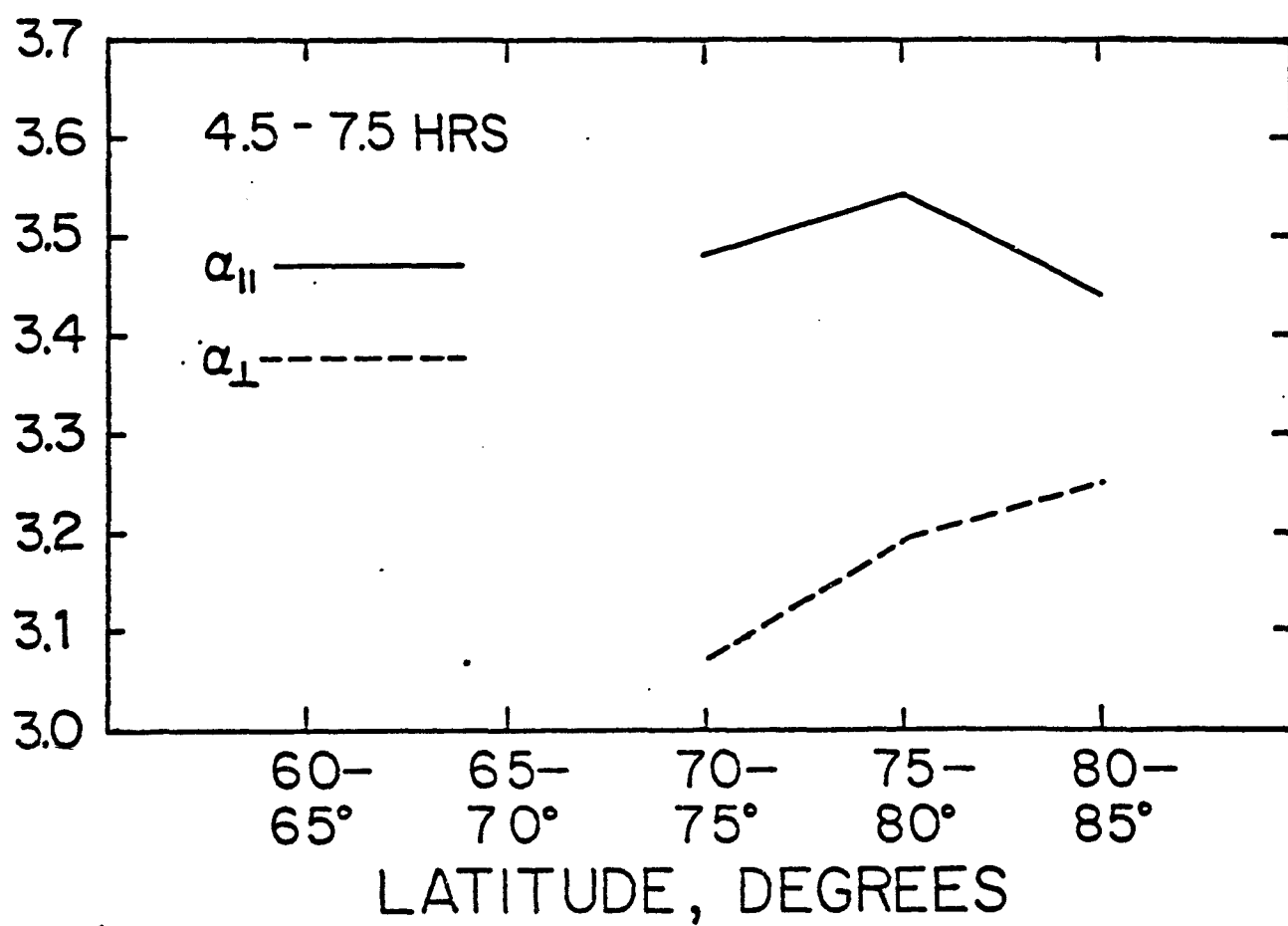


Figure 4c



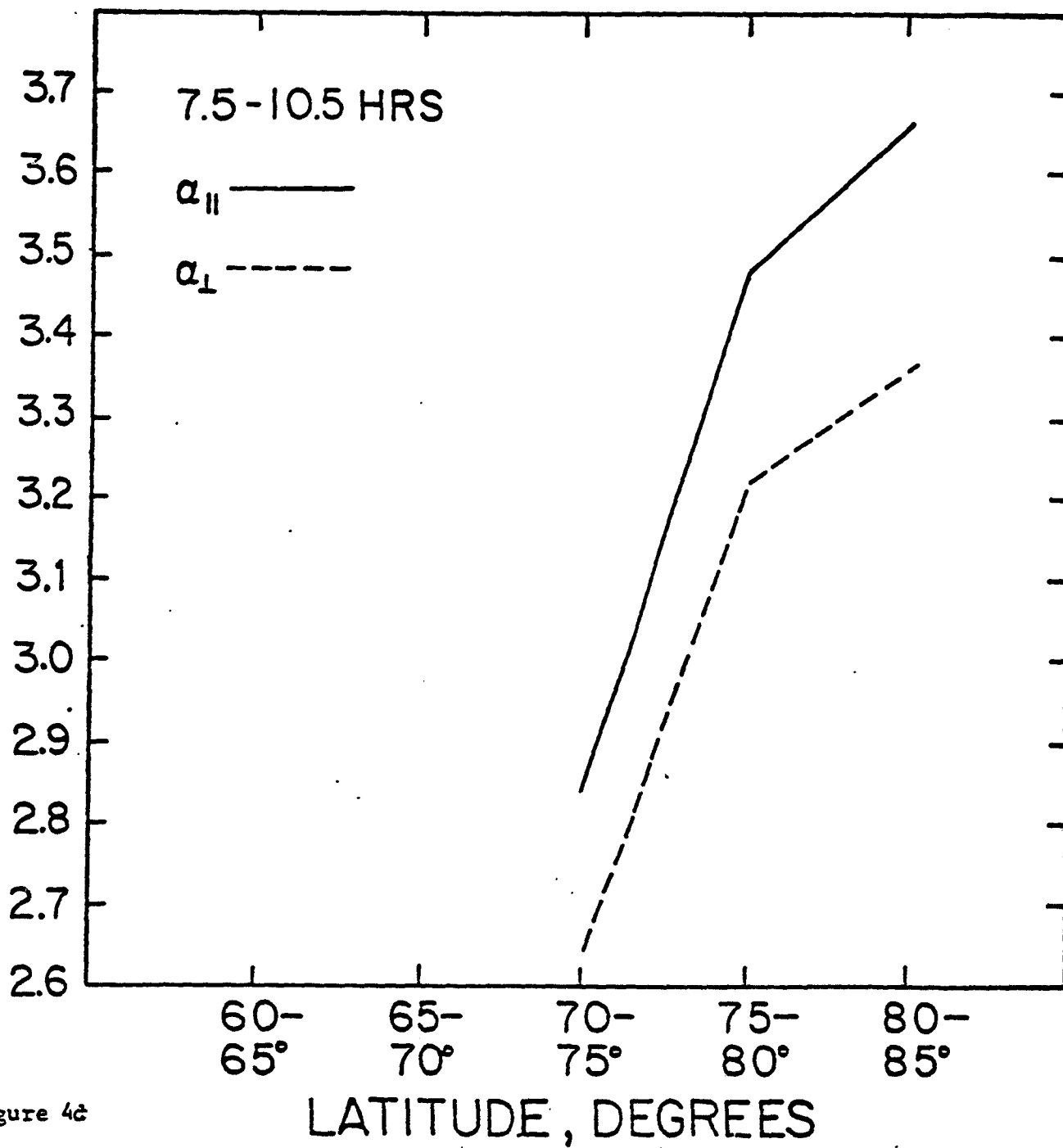


Figure 4c

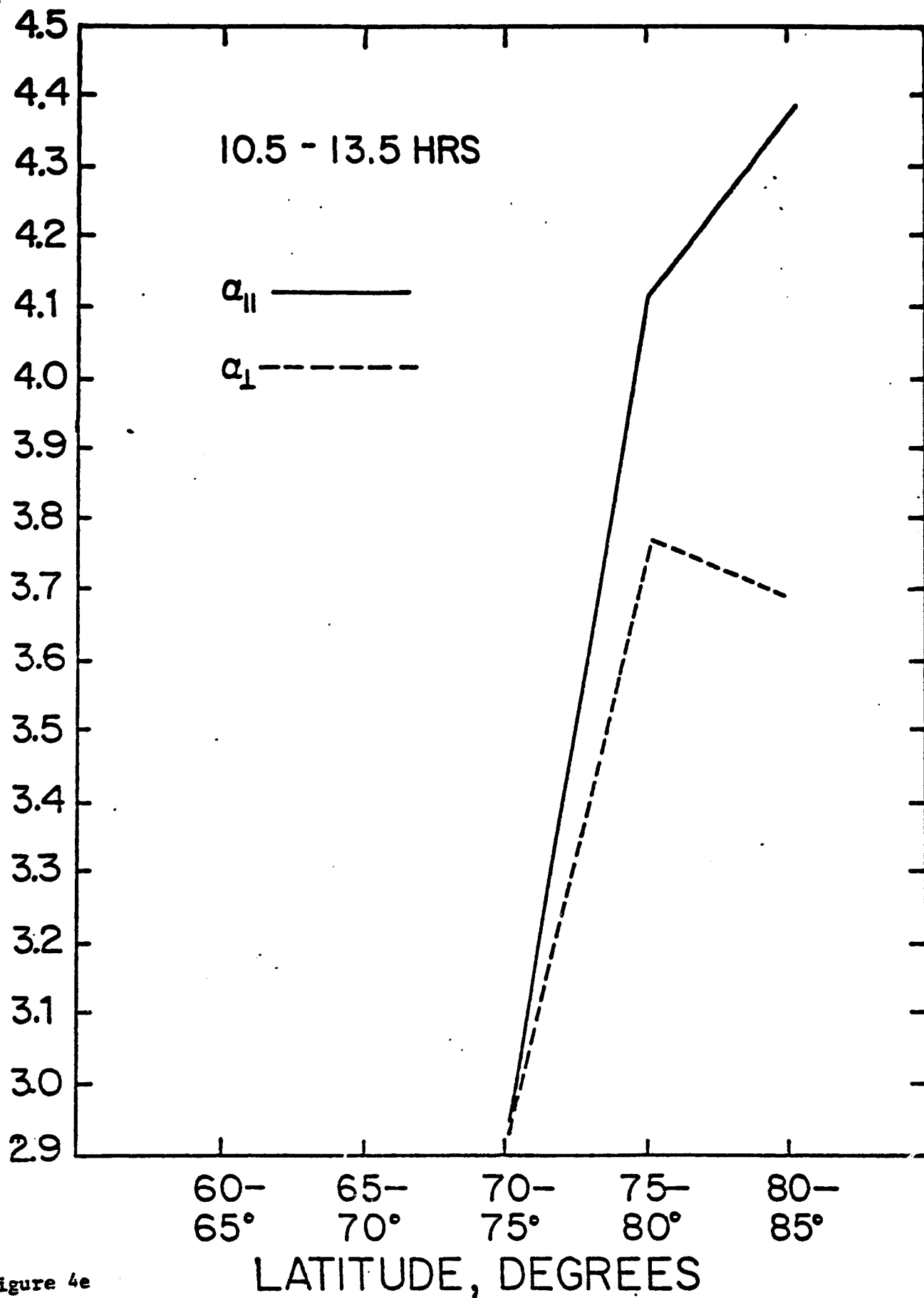


Figure 4e

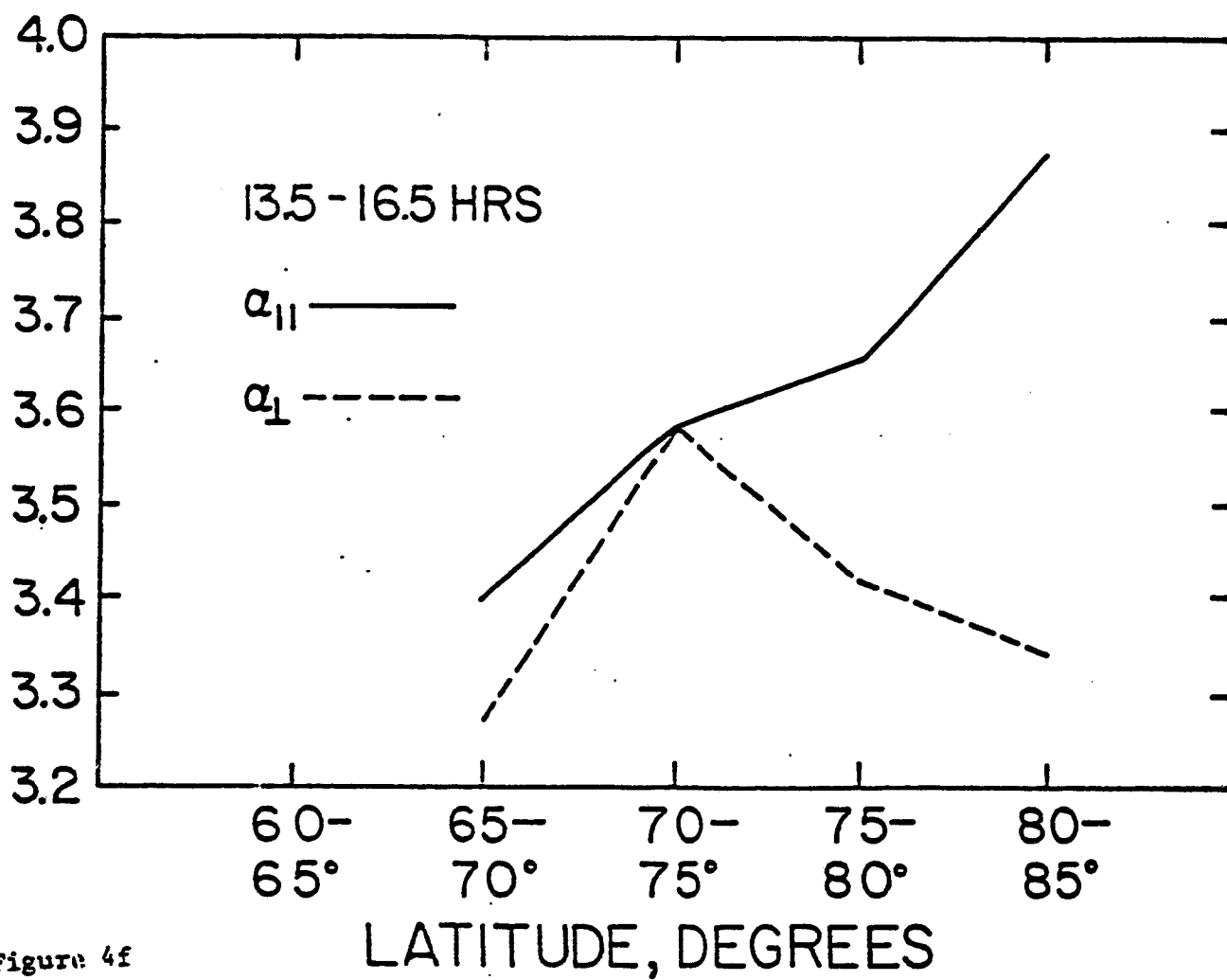


Figure 4f

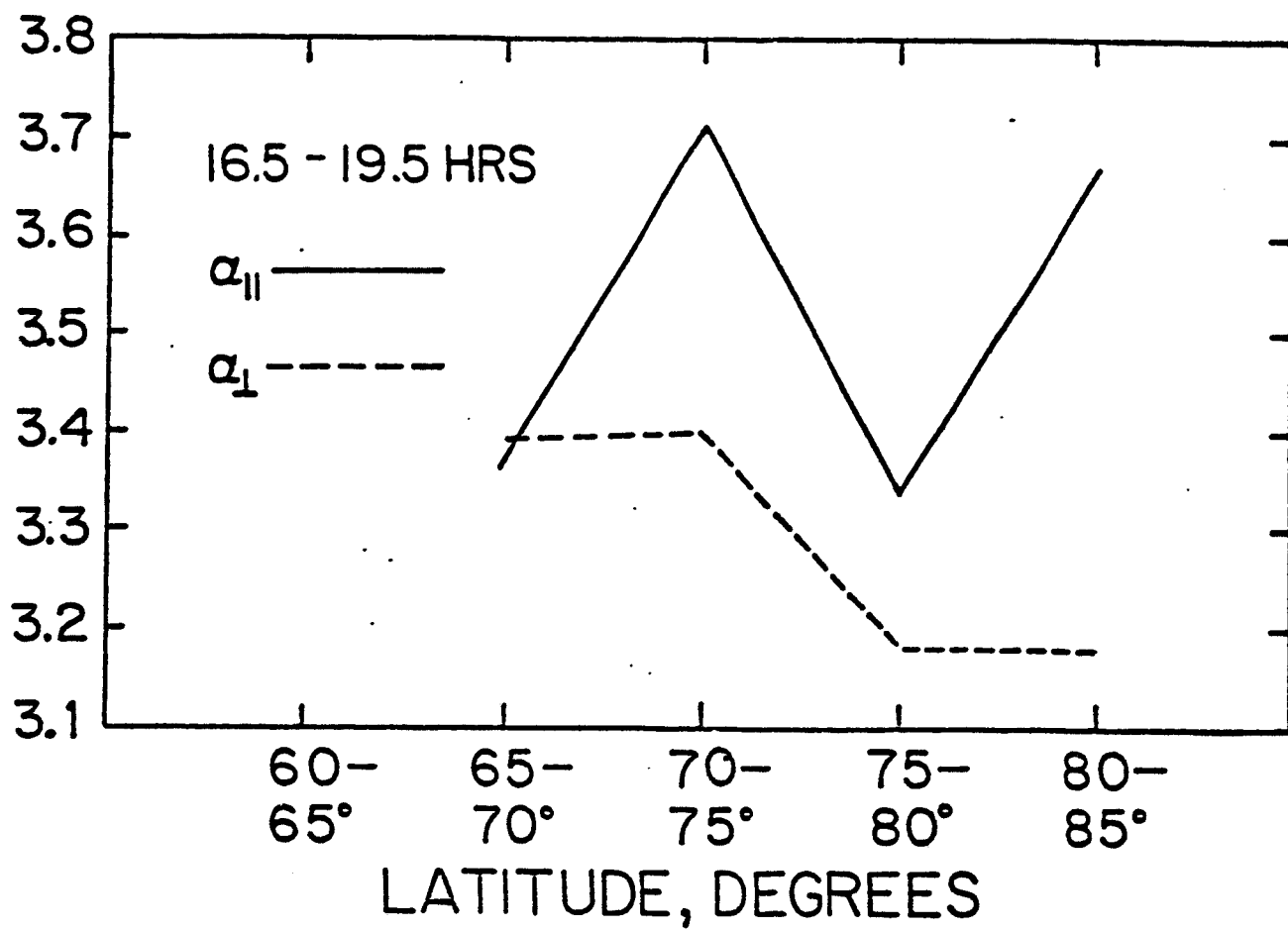


Figure 4g

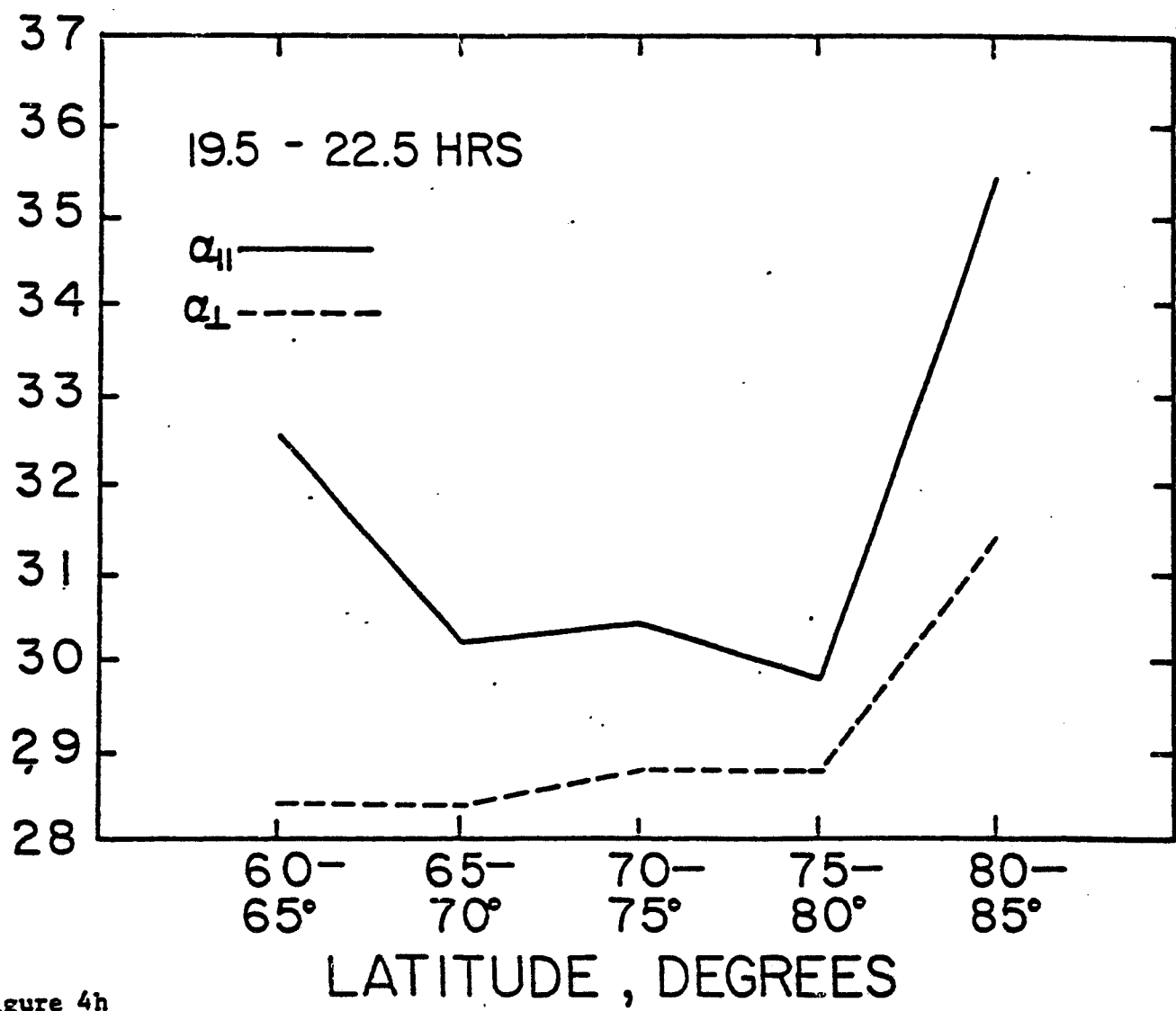


Figure 4h

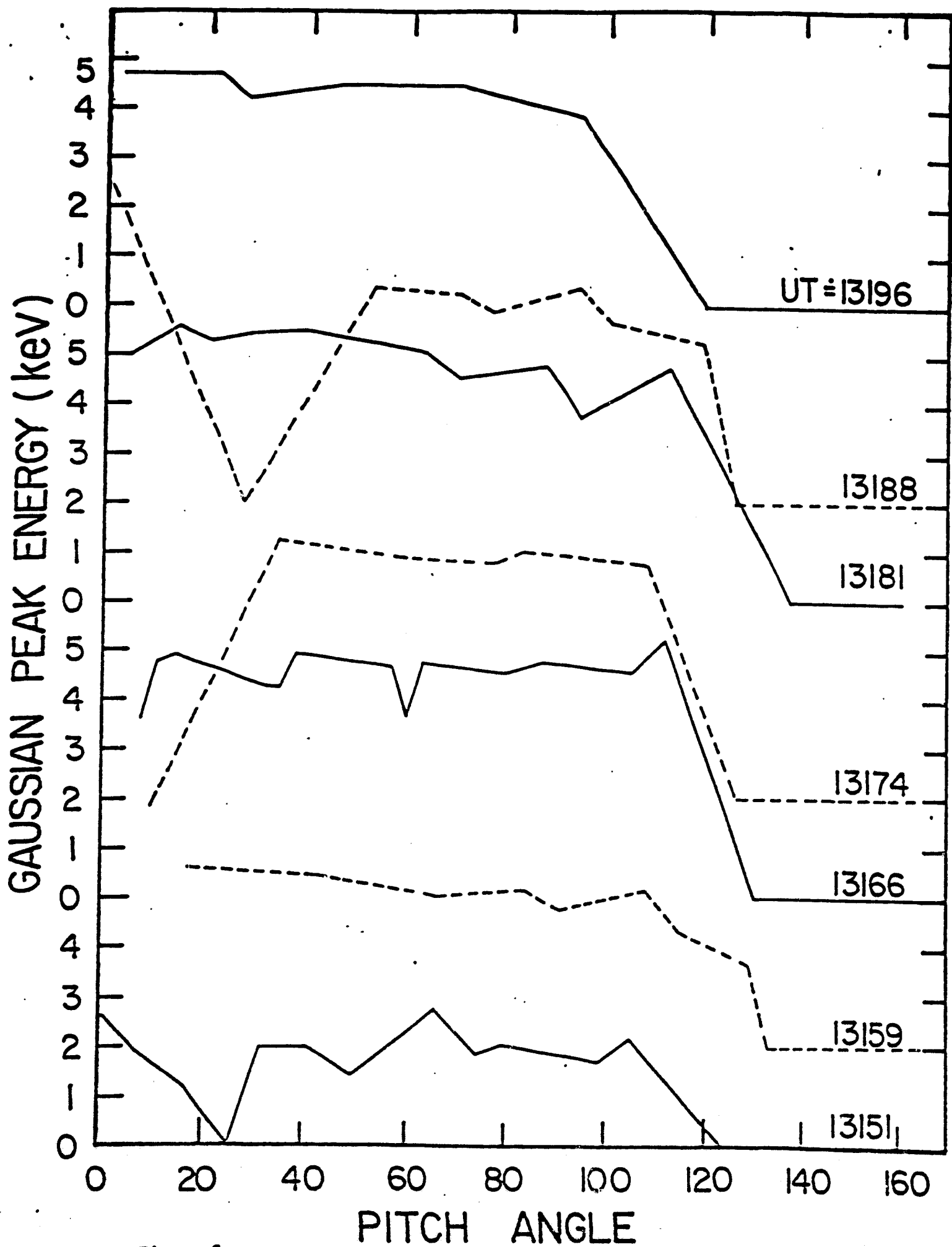
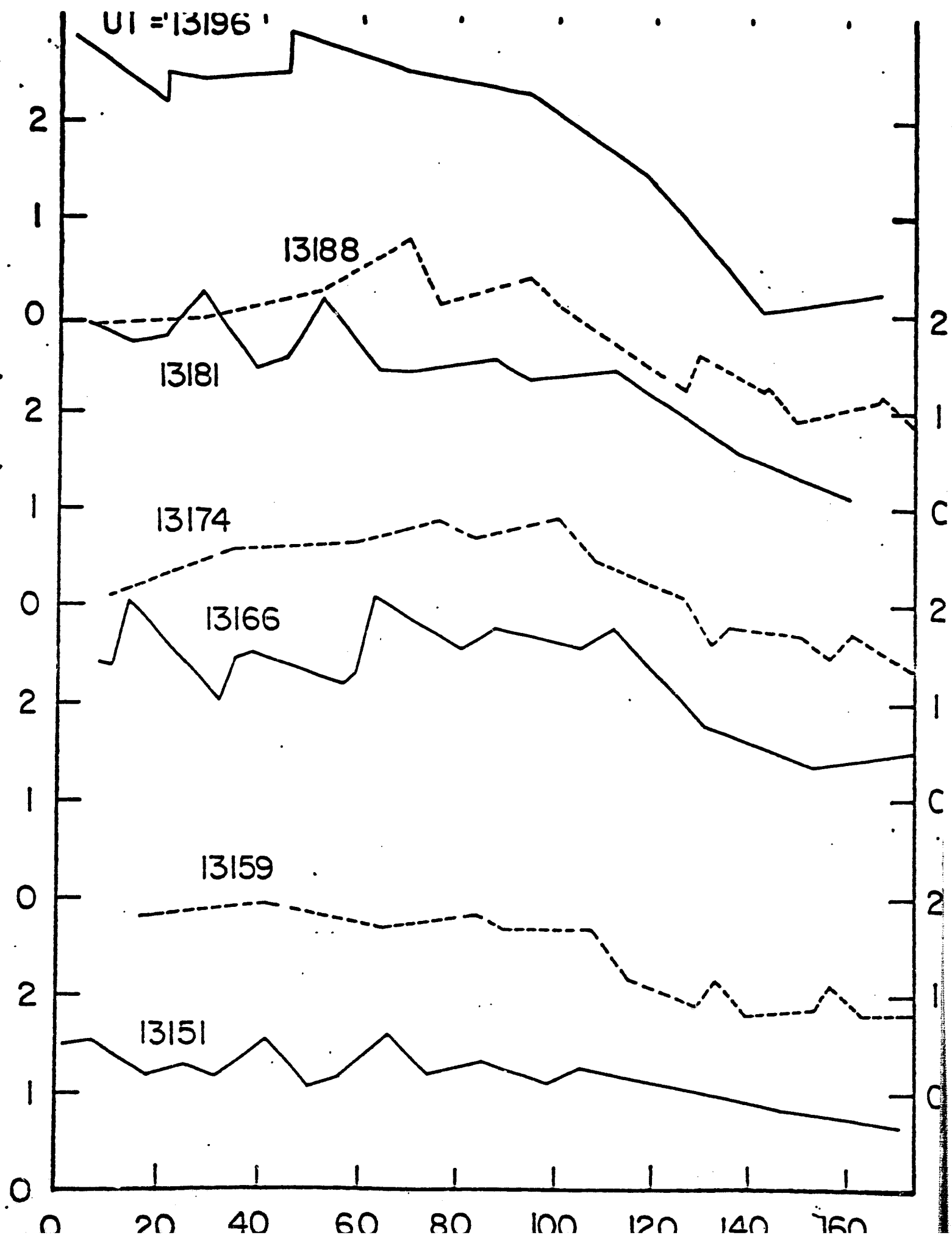


Figure 5

BEAM TEMPERATURE (keV)



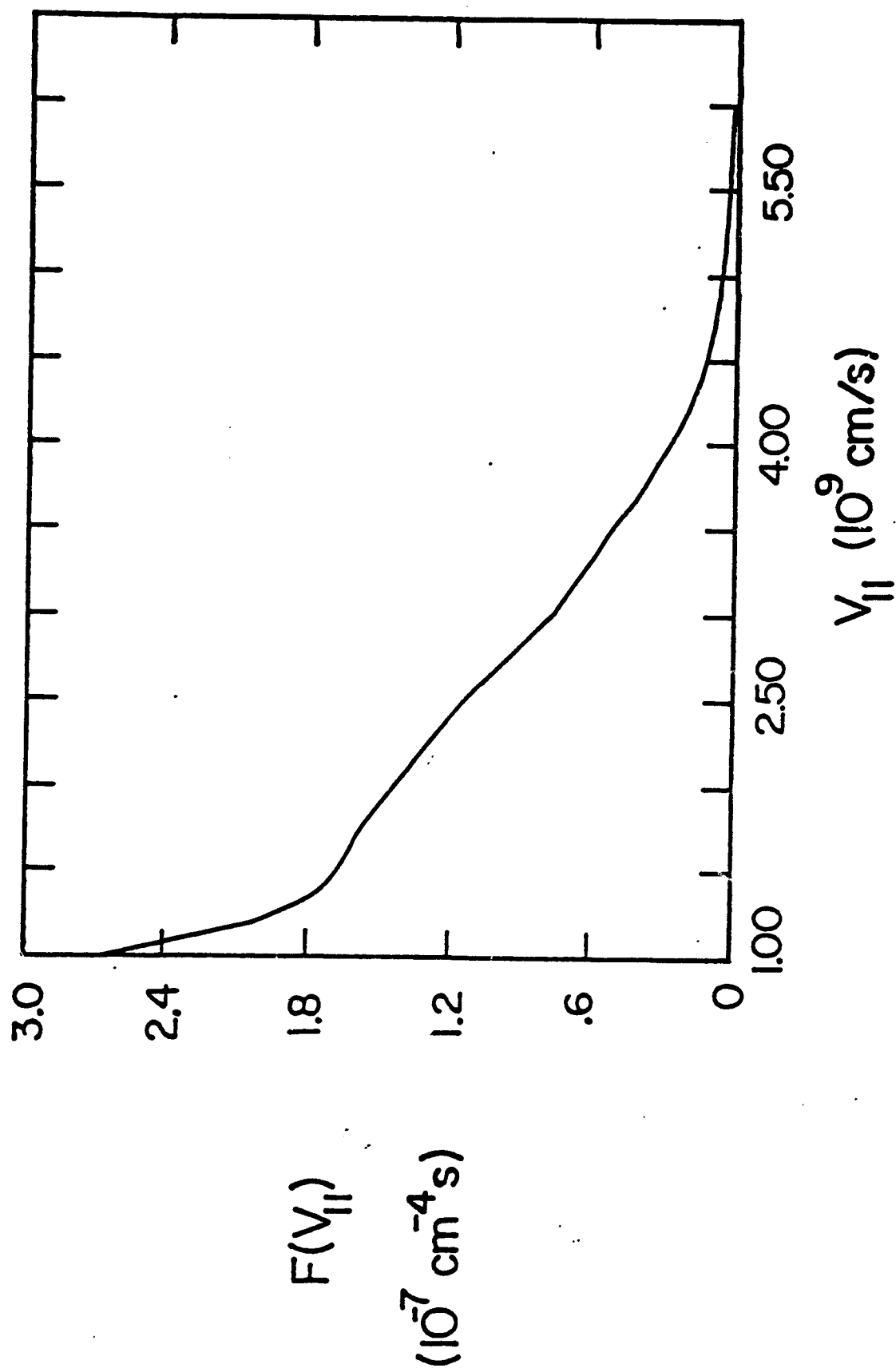


Figure 7



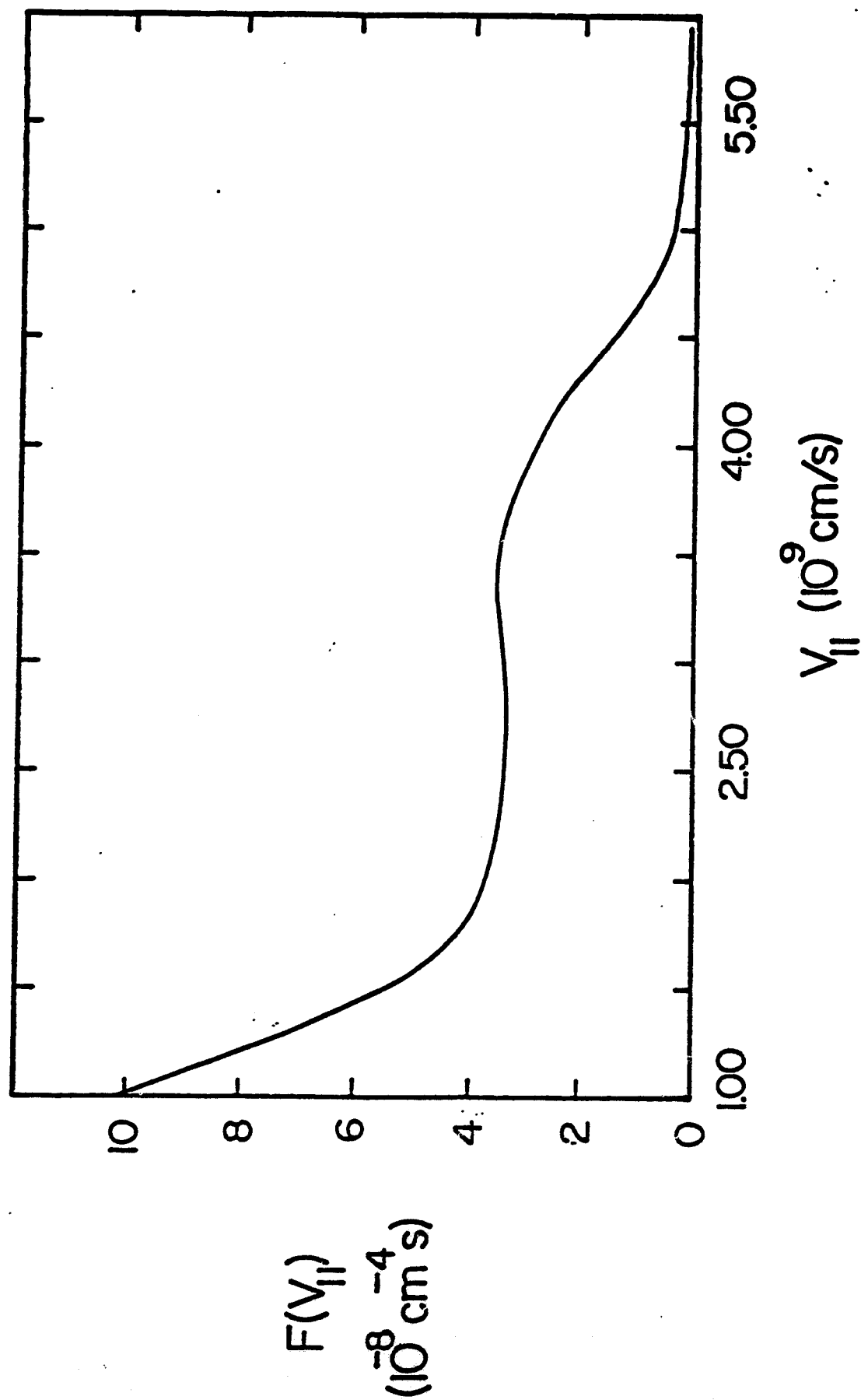


Figure 8

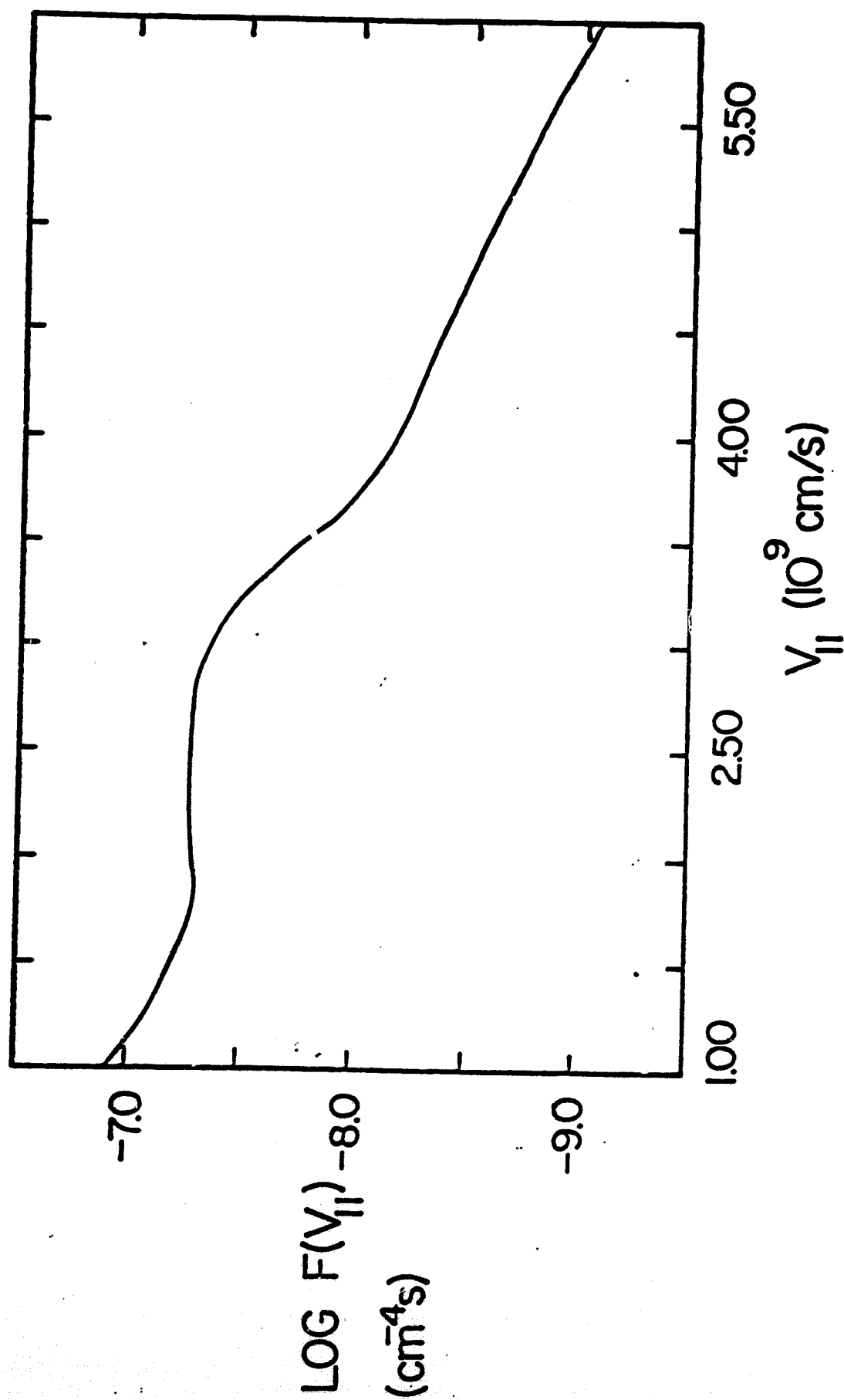


Figure 9

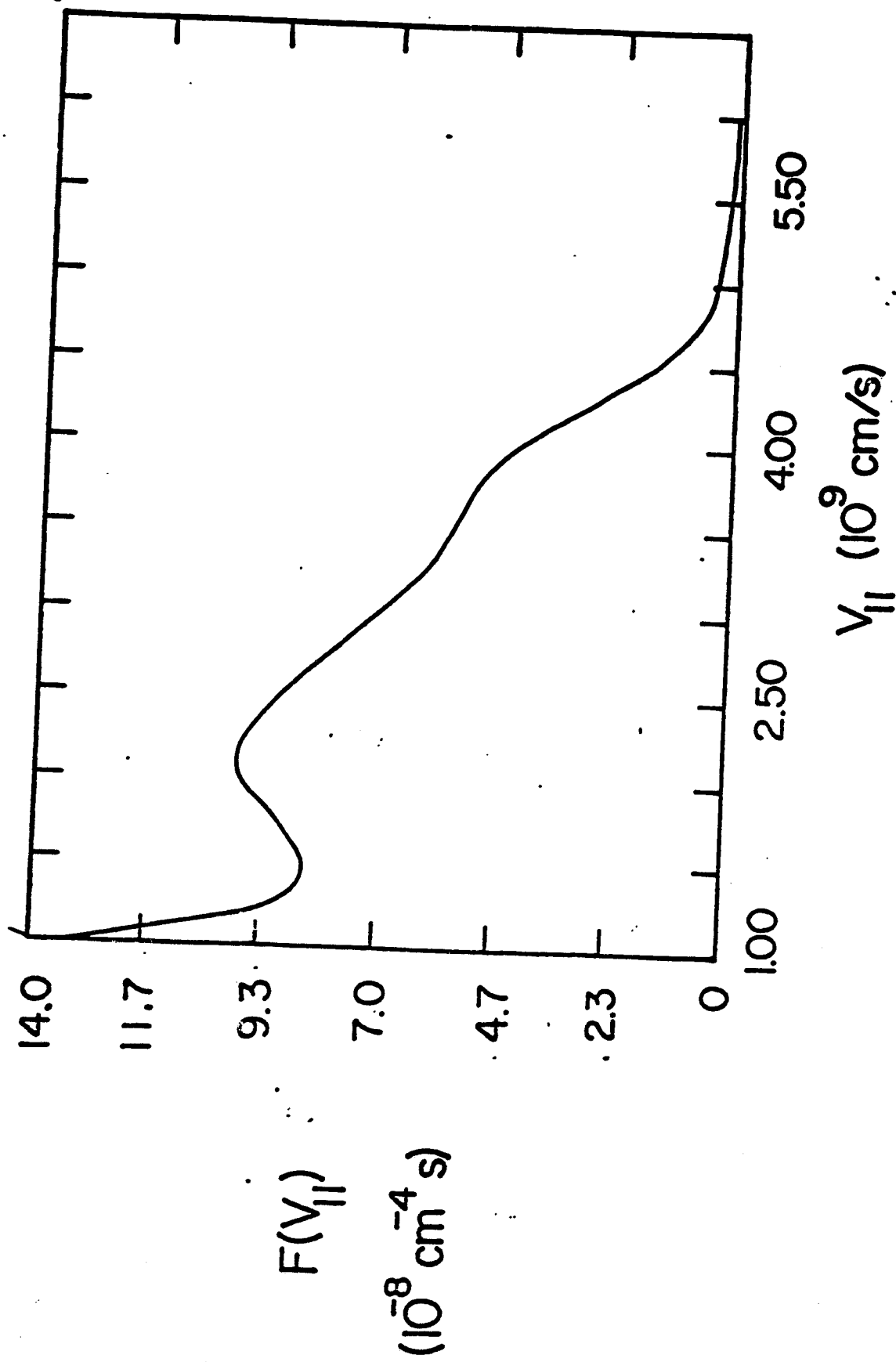


Figure 10

## Appendix I. Curve Fitting Procedure

The curve fitting procedure involves a linear least squares fitting to the electron flux spectrum using a superposition of three functions.

$$F_c(E) = F_{c1}(E) + F_{c2}(E) + F_{c3}(E)$$

where  $F_c$  is the electron flux and  $E$  the energy. The forms of the functions used are:

### Power law

$$F_{c1}(E) = P_1 E^{(1 + P_2)}$$

### Maxwellian

$$F_{c2}(E) = Cn_b \frac{E}{(kT_b)^{3/2}} \exp\left(-\frac{E}{kT_b}\right)$$

where  $C$  is a constant,  $n$  is the density and  $T_b$  is the temperature.

### Gaussian

$$F_{c3}(E) = E \exp\left[-\left(\frac{E - P_2}{P_1}\right)^2 + P_3\right]$$

The actual fitting is performed in  $\log_e$  space using the functions in the forms:

### Power law

$$\log_e(F_{c1}/E) = X_1 + X_2 \log_e E$$

where  $P_1 = \exp(X_1)$

$$P_2 = X_2$$

### Maxwellian

$$\log_e(F_{c2}/E) = Y_1 + Y_2 E$$

where  $kT_b = -1/X_2$

$$n = \exp(X_1) \frac{(kT_b)^{3/2}}{C}$$

### Gaussian

$$\log_e(F_{c3}/E) = X_1 E^2 + X_2 E + X_3$$

where  $P_1 = \frac{1}{\sqrt{-X_1}}$

$$P_2 = \frac{-X_2}{2X_1}$$

$$P_3 = - \left( \frac{X_2^2 - 4X_1X_3}{4X_1} \right)$$

The fitting is performed in such a way that it is possible to fit a particular electron flux spectrum with any one of the three given functions separately or with any combination of the three. The basic procedure is to compute the least squares fit, compute the error between the observed spectrum and computed spectrum and select the least squares fit with the smallest error. The error is given by the formula,

$$\text{ERROR} = \frac{1}{N - h_p - 1} \sum_{i=1}^N \{ \log_{10}[F_o(E_i)] - \log_{10}[F_c(E_i)] \}^2$$

where, N is the number of data points used in the fitting

$h_p$  is the number of non-zero parameters in the fit

$F_c$  is the computed flux

$F_o$  is the observed flux

$E_i$  is the energy corresponding to the  $i^{\text{th}}$  data point.

The first step in the fitting routine is to fit the entire spectrum to the power law function and the Maxwellian function separately and choose the best fit. Next the routine searches for the optimal fit for a superposition of these same two functions. This search is accomplished by fitting the data points

corresponding to energies  $E_k$  through  $E_{16}$  ( $=E_{\text{max}}$ ) to the Maxwellian function, subtracting the results from the observed flux values and fitting the remainder to the power law function. The two fits are then added, the error is computed and compared to the previous least error and the best fit chosen. This procedure is repeated for  $k$  ranging from  $k = 3$  to  $k = 13$ .

To check for the presence of a monoenergetic peak (approximated by a Gaussian function) the spectrum representing the best fit from the above search is scanned in the energy range  $E_3$  to  $E_{13}$  to locate three consecutive flux values which lie above the computed spectrum. If three or more such points are found, they are deleted from the observed spectrum and the procedure outlined above is repeated for this adjusted spectrum. The points lying above the original best fit which were deleted are fit to a Gaussian function and added to the recomputed power law plus Maxwellian fit. The error is then found and compared to the original best fit. The fit with the least error is then taken as the overall best fit to the data and the parameters are stored in the output file.

## Appendix II. One-Dimensional Hump of an Isotropic Three-Dimensional Distribution

Let the one-dimensional distribution function  $F(v_z)$  have a maximum at  $v_{zm}$ .

Let the three-dimensional distribution function be isotropic,  $f(v^2)$ , where  $v^2 = v_x^2 + v_y^2 + v_z^2$ .  $F(v_z)$  and  $f(v^2)$  are related by the expression

$$F(v_z) = \int_{-\infty}^{\infty} \int_{-\infty}^{\infty} f(v^2) dv_x dv_y. \quad (A.1)$$

**Theorem:**  $v_{zm}$  has always the value 0 irrespective of the shape of  $f(v^2)$ , and this is the only value it can have.

**Proof:**

A necessary condition for a maximum of  $F(v_z)$  is

$$\begin{aligned} \frac{d}{dv_z} F(v_z) \Big|_{v_{zm}} &= \int_{-\infty}^{\infty} \int_{-\infty}^{\infty} \frac{\partial}{\partial v_z} f(v^2) \Big|_{v_z=v_{zm}} dv_x dv_y = 0 \\ 2v_{zm} \int_{-\infty}^{\infty} \int_{-\infty}^{\infty} \frac{d}{d(v^2)} f(v^2) \Big|_{v_z=v_{zm}} dv_x dv_y &= 0 \end{aligned}$$

Let us assume that  $v_{zm} \neq 0$ . Then

$$\int_{-\infty}^{\infty} \int_{-\infty}^{\infty} \frac{d}{d(v^2)} f(v^2) \Big|_{v_z=v_{zm}} dv_x dv_y = 0$$

Introduce polar coordinates in the  $v_x v_y$ -plane

$$v_x = v_{\perp} \cos \phi$$

$$v_y = v_{\perp} \sin \phi$$

$$v^2 = v_{\perp}^2 + v_{zm}^2$$

Then we obtain (since  $\frac{d}{d(v^2)} = \frac{d}{d(v_\perp^2)}$ )

$$\int_0^\infty du \int_0^{2\pi} d\theta u \frac{d}{d(v_\perp^2)} f(v_\perp^2 + v_{zm}^2) = 0$$

$$\int_0^\infty d(v_\perp^2) \frac{d}{d(v_\perp^2)} f(v_\perp^2 + v_{zm}^2) = 0$$

$$f(\infty) - f(v_{zm}^2) = 0$$

Since  $f(\infty) = 0$ , this implies

$$f(v_{zm}^2) = 0. \quad (A.2)$$

Because of the isotropy of  $f$  it follows that  $f(v^2)|_{v^2=v_{zm}^2} = 0$ . Since the function  $f(v^2)$  is by definition non-negative, it can vanish at the point  $v^2 = v_{zm}^2$  only if

$$\frac{d}{d(v^2)} f(v^2) \Big|_{v^2=v_{zm}^2} = 0. \quad (A.3)$$

Hence, we conclude that

$$\frac{d}{dv_z} F(v_z) \Big|_{v_z=v_{zm}} = 0 \quad \text{with } v_{zm} \neq 0$$



only if

$$\left. \frac{d}{d(v^2)} f(v^2) \right|_{v^2 = v_{zm}^2} = 0.$$

In order to determine whether  $F(v_z)$  actually has a maximum at  $v_{zm}$  we have to look at the second derivative.

$$\begin{aligned} \frac{d^2}{dv_z^2} F(v_z) &= \frac{d}{dv_z} \int_{-\infty}^{\infty} \int_{-\infty}^{\infty} \frac{\partial f}{\partial v_z} dv_x dv_y \\ &= 2\pi \frac{d}{dv_z} v_z \int_0^{\infty} \frac{df}{d(v_1^2)} d(v_1^2) \end{aligned}$$

$$v^2 = v_1^2 + v_z^2$$

$$\begin{aligned} &= -2\pi \frac{d}{dv_z} [v_z f(v_z^2)] \\ &= -2\pi [f(v_z^2) + v_z \frac{d}{dv_z} f(v_z^2)] \\ &= -2\pi [f(v_z^2) + 2v_z^2 \frac{d}{d(v^2)} f(v^2)] \end{aligned}$$

which vanishes at  $v^2 = v_{zm}^2$  according to equations (A.2) and (A.3). Hence, there cannot be a maximum at  $v_{zm} \neq 0$ . If  $f(v_x, v_y, v_z)$  is spherically symmetric and if  $F(v_z)$  has a maximum, it can occur only at  $v_z = 0$ . q.e.d.